Chapter 12
High-Temperature Samarium Cobalt Permanent Magnets

Oliver Gutfleisch

Abstract This chapter reviews the development of SmCo-type magnets over the last 40 years. First, the physical metallurgy and crystal structures are considered; then the focus is on the recent developments in high-temperature $\mathrm{Sm(Co_{bal}Fe_{w}Cu_{x}Zr_{y})_{z}}$ magnets suitable for operation temperatures up to 500°C. It is elucidated that the evolution of coercivity and microchemistry in the respective phases of the heterogeneous nanostructure as well as magnetic domain structure is very sensitive to details of the processing procedure, especially to the slow cooling ramp as the last step where the hard magnetic properties evolve. These changes give rise to rather complex pinning mechanisms in a three-phase precipitation structure, which again depend in a subtle manner on the microchemistry of the 1:5-type cell boundary phase in the 2:17-type magnets. It is the amount and distribution of Cu in and at the cell boundary phase which is the prevalent factor determining the pinning strength and which can yield a non-monotonic temperature dependence of coercivity. The chapter concludes with an overview of novel non-equilibrium processing routes used to obtain SmCo-type nanocomposites.

12.1 Introduction

The last century has been the golden age of permanent magnetism, and the progress in the field of permanent magnets has been dramatic over the last 40 years. Permanent magnets are widely used in our daily life and feature in a large variety of domestic products such as quartz analogue watches, earphones, microwaves, cordless tools, mobile phones, and voice coil motors. A modern car, for example, contains at least 50 permanent magnets. In this case, most of the magnets are so-called hard ferrites ($\mathrm{BaFe_{12}O_{19}}$ and $\mathrm{SrFe_{12}O_{19}}$), a low cost–low performance type of

---

O. Gutfleisch (✉)
Leibniz Institute for Solid State and Materials Research (IFW Dresden), Institute for Metallic Materials, Helmholtzstr. 20, 01069 Dresden, Germany
e-mail: o.gutfleisch@ifw-dresden.de

J.P. Liu et al. (eds.), *Nanoscale Magnetic Materials and Applications*,
DOI 10.1007/978-0-387-85600-1_12,

magnet. In more sophisticated applications, where, e.g., miniaturization is an issue or completely new designs are needed, high-performance permanent magnets based on rare earth–transition metal compounds are used. $Nd_2Fe_{14}B$, generating a field of the order of 1 T, is mostly used in computer or portable electronic devices, but also in medicine for (intraoperative) diagnostics using a magnetic resonance imaging apparatus. Other examples for new applications are hybrid electric vehicles (HEV), electronic cyclotronic resonance ion source, magnetic refrigeration, and wind generators. Modern high-performance magnets are based on compounds of a magnetic light rare earth (Pr, Nd, Sm) for strong magnetic anisotropy and a 3d element (Fe, Co) for large magnetization and high Curie temperature. A favorable combination of these values is only a prerequisite for a good hard magnetic material; the ultimate suitability can only be gauged when coercive field H_c, remanent magnetization B_r, and maximum energy density $(BH)_{max}$, as the most relevant extrinsic properties, fulfill certain criteria. This is done by the preparation of appropriate microstructures with typical length scales of 1 nm to 100 μm (for more detailed descriptions the reader is referred to overviews by Cullity [14], Gavigan and Givord [29], Coey [12], Chikazumi [11], Strnat [95, 96], Buschow [5, 6], Skomski and Coey [88], Gutfleisch [39, 41], and Khlopkov et al. [53]).

The intrinsic magnetic properties are determined by magnetic moments and interactions on an atomic scale and are independent of the microstructure of the specific material. In rare earth–transition metal (R–T) compounds three types of exchange interactions occur: T–T, R–T, and R–R. In the case of $SmCo_5$, for example, where the transition metal carries a well-established magnetic moment, the T–T interactions dominate. The strong ferromagnetic coupling is responsible for the magnetic order up to very high Curie temperature. The R–R exchange coupling proceeds indirectly via 4f–5d–5d–4f and is generally very small compared to the R–T interaction. The latter proceeds also via an indirect mechanism (4f–5d–3d) in which the strong interatomic direct 5d–3d exchange is transmitted to the 4f electrons via the intra-atomic 4f–5d ferromagnetic interaction. The 5d–3d exchange is antiferromagnetic when the 5d band is less than half full and the 3d band is more than half full as it is the case for compounds of rare earths with ferromagnetic 3d metals. Qualitatively it can be summarized that as the transition metal spin S_T couples antiparallel to the rare earth spin S_R, the magnetizations of R and T sublattices couple parallel for the light rare earth elements ($J = L - S$) and antiparallel for the heavy rare earth elements ($J = L + S$) according to Hund's rule. The orbital magnetic moments in rare earth metals remain unquenched by crystalline fields because the magnetic moments are produced by 4f electrons well inside the atoms and protected from the surrounding atoms. However, the electrostatic crystalline electric field acting on the non-spherical 4f charge distribution favors a certain orientation of its preferred axis and thus also directions of the magnetization. The result of this interaction is an enormous magnetocrystalline anisotropy. The rare earth series presents an incomplete filling of the 4f shell. The number of electrons in the inner 4f shell vary from 0 to 14 through the series La (atomic number in the periodic table: $Z = 57$) to Lu ($Z = 71$). The total magnetic moment of an R atom has both orbital and spin components. However, the 4f shell is not the outermost shell of the atom. The R–R exchange coupling between two R atoms in a solid is indirect because the direct overlap between the 4f shells of adjacent rare earth atoms is negligible. The resulting weak magnetic interaction with the 4f electrons of neighboring atoms causes the low Curie temperatures of the rare earth metals; in fact only Gd ($T_C = 16°C$) is ferromagnetic close to room temperature.

Microwave tubes, gyroscopes and accelerometers, reaction and momentum wheels to control and stabilize satellites, magnetic bearings, sensors, and actuators are examples of applications where high-energy density magnets with magnetic fields stable over a variety of environmental conditions and wide temperature ranges are required. $SmCo_5$- and Sm_2Co_{17}-type magnets [3, 57, 83, 84, 94, 95] are ideal for these applications because of their high magnetocrystalline anisotropy and Curie temperature. Standard commercial magnets of these types satisfy these requirements over the temperature range from 50 to 250°C. In addition, they exhibit a high corrosion resistance; their disadvantages are the costly raw materials and the difficult magnetization. A slight increase in temperature stability can be achieved when substituting heavy rare earth elements for Sm [111]. Even better temperature coefficients of remanence ($\alpha = dM_r/dT$) and coercivity ($\beta = dH_c/dT$) are required for higher operating temperatures above 450°C [43, 100], which are needed for rare earth permanent magnets (RPMs) for electric vehicles, hybrid magnetic bearings for turbine engines and advanced power systems. The availability of these newly developed magnets could also open completely new applications such as magnetic brakes with performance close to normal friction brakes.

12.2 Physical Metallurgy and Crystal Structures

SmCo phases show a variety of crystal structures and these alloys have been studied for more than 40 years now. Here, the focus is on the SmCo binaries with Curie temperatures surpassing 400°C and which are stable at room temperature, or which can be easily retained at room temperature in a metastable state by quenching from higher temperatures. Their crystal structure data are shown in Table 12.1. Note that the 1:7- and the 1:5-type structures are closely related to each other and have the same space group *P6/mmm* [4]. The rhombohedral Th_2Zn_{17} structure can be derived from the $SmCo_5$ structure by an ordered substitution of a dumbbell of Co atoms for one-third of the Sm atoms. When a random substitution by Co pairs occurs, a

Table 12.1 Crystal structure data of SmCo binaries [3]

Compound	Lattice constant (nm)	Structure type	Space group
$SmCo_5$	a=0.5002 c=0.3964	$CaCu_5$	*P6/mmm*
Sm_2Co_{17}	a=0.4856 c=0.4081	$TbCu_7$	*P6/mmm*
Sm_2Co_{17}	a=0.8360 c=0.8515	Th_2Ni_{17}	Pb_3/mmc
Sm_2Co_{17}	a=0.8395 c=1.2216	Th_2Zn_{17}	$R3m$

disordered Co-rich phase of $TbCu_7$ is formed [52]. This phase becomes unstable when 22% of Sm atoms have been replaced by Co pairs resulting in a phase separation into the two neighboring phases, $SmCo_5$ and Sm_2Co_{17}.

Figure 12.1 shows the structures of the RCo_5 and R_2Co_{17} compounds. Depending on the stacking sequence of the mixed SmCo planes one distinguishes the rhombohedral Th_2Zn_{17} (ABCABCABC . . .) and the hexagonal Th_2Ni_{17} (ABABAB . . .) modifications. The Co-rich part of the SmCo equilibrium phase diagram shown in Fig. 12.2 illustrates the congruent melting of Sm_2Co_{17} at 1,338°C and the peritectic reaction at 1,292°C to form $SmCo_5$.

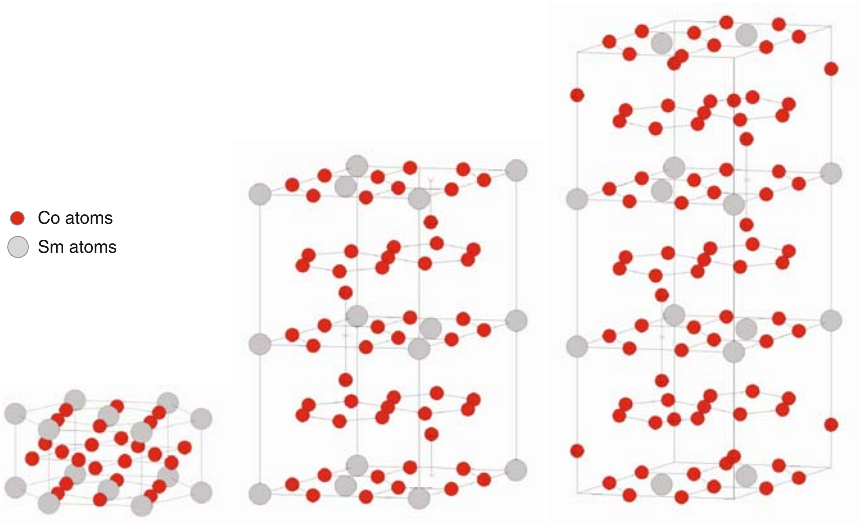

$SmCo_5$
$CaCu_5$-type, hexagonal

Sm_2Co_{17}
Th_2Ni_{17}-type, hexagonal

Sm_2Co_{17}
Th_2Zn_{17}-type, rhombohedral

Fig. 12.1 Structures of the RCo_5 and R_2Co_{17} compounds (after [26])

The used terminology of "1:5"- and "2:17"-type magnets is rather simplistic; in fact the real magnets are multiphase magnets with a complex sequence of annealing steps and, especially in the case of 2:17, a heterogeneous nanostructure.

Both the 1:5 and the 2:17 types are usually produced via the powder metallurgical sintering route. Unlike the $Nd_2Fe_{14}B$ phase, the hexagonal $SmCo_5$ compound [94] with the $CaCu_5$ structure shows a relatively large homogeneity region in the SmCo phase diagram [7, 90, 91] as shown in Fig. 12.2. This region, however, becomes asymmetric when approaching the peritectic melting temperature of 1,292°C. The 2:17 type shows currently the best temperature coefficients α and β of all RPMs, and its hard magnetic properties are achieved by an elaborate series of heat treatments resulting in a complex microstructure. Commercially produced SmCo-type sintered magnets based on the 2:17R-type phase (with the rhombohedral (R) Th_2Zn_{17}-type structure) have usually a composition close to $Sm(Co,Fe,Cu,Zr)_{7.5}$. The homogeneity region of the 2:17R phase narrows with decreasing temperature [7, 79], and a fine cellular precipitation structure develops from the single-phase metastable

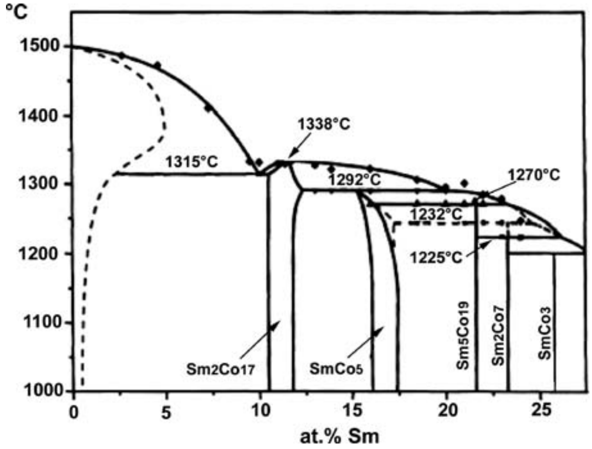

Fig. 12.2 SmCo phase diagram. Reproduced with permission of Elsevier from [7]

precursor, obtained by solid solution treatment at ~1,200°C, quenching and subsequent annealing at ~800°C, and slow cooling to 400°C (Fig. 12.3). The structure of the homogenized high-temperature phase has been described differently. Whereas Rabenberg et al. [81, 82] assumed the hexagonal (H) Th_2Ni_{17}-type structure (2:17H), it has been reported later that the hexagonal $TbCu_7$-type structure (1:7H) is more realistic and, after quenching from ~1,200°C, the material consists of the supersaturated 1:7H phase with partial 2:17R-type order [68]. According to these authors the 2:17R cells originate from nucleation and growth out of the 1:7 structure. This induces a related increase of Cu (according to Perry [79] the solubility of Cu in 2:17R at 850°C is only 4 at.%) and Sm contents in the surrounding 1:7 matrix, which tends to 1:5 stoichiometry and forms the cell boundaries that have a thickness of 5–10 nm (note that the 1:7- and the 1:5-type structures have the same space group *P6/mmm* [4]). A similar scenario had been already proposed by Livingston and Martin [66] who, however, speak of a disordered 1:5 structure instead of the 1:7 structure as the homogenized high-temperature phase. The development of the specific form of the cellular precipitation structure is governed by the elastic energy due to lattice misfit of the 1:5 and the 2:17R phases. The cell interior (cell diameter of typically 100 nm) has the 2:17R-type structure and shows boundaries of coherent twins in the basal plane [27, 28]. The 2:17R phase is the majority phase of the material. The 1:5 cell boundary phase is coherent (or at least semi-coherent) with the cell interior [66].

A so-called platelet phase (also referred to as lamellar or Z-phase) rich in Zr is observed additionally parallel to the 2:17R basal plane. In Fig. 12.4, this Z-phase manifests itself as thin lines extending over many 2:17R cells. The reported thickness of the lamellae is very small ranging from 1 nm [68] to 3 nm [42]. The lattice structure of the Z-phase is still somewhat controversially discussed. Rabenberg et al. [81, 82] reported the rhombohedral Be_3Nb-type structure, which has been confirmed by Maury et al. [68], Xiong et al. [102], and Stadelmaier et al. [92]. On the other hand, Fidler and Skalicky [27, 28] found the 2:17H-type structure for the Z-phase, which is accepted by various authors (e.g., [35]). The Z-phase is considered to stabilize the cellular microstructure and to provide diffusion paths for Cu, Fe, and Co, thereby modifying phase-ordering kinetics [81, 82].

Fig. 12.3 Schematic heat treatment regime for precipitation-hardened Sm_2Co_{17}-type magnets

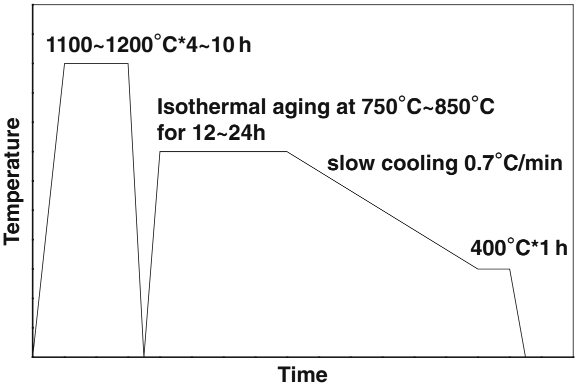

In order to optimize Sm_2Co_{17}-type magnets for a particular high-temperature application, the profound knowledge of the effects of alloying elements is necessary (the quinary Sm–Co–Fe–Cu–Zr phase diagram has been studied by Lefèvre et al. [59]). It has been shown that Cu and Zr stabilize the $SmCo_7$-type phase and Fe favors the Sm_2Co_{17}-type phase with Th_2Zn_{17} structure [70]. The substitution of Co by Fe results in the precipitation of a Co–Fe phase and in a reduction of coercivity but improved saturation magnetization [76–78]. This undesired precipitation can be reduced by the addition of small amounts of Zr [74]. Cu induces the precipitation of the $SmCo_5$ cell boundary phase surrounding the Sm_2Co_{17}-R cells [66, 71]. Cu is considered to have complete solubility in $SmCo_5$ and to stabilize this structure, in

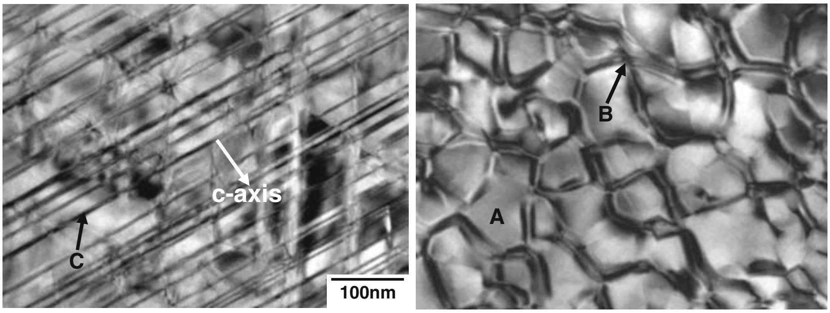

Fig. 12.4 TEM bright field images of a $Sm(Co_{0.784}Fe_{0.100}Cu_{0.088}Zr_{0.028})_{7.19}$-sintered magnet with the nominal c-axis of the 2:17R main phase parallel (*left*) and perpendicular (*right*) to the imaging plane (A indicates the 2:17R type, B the 1:5-type cell boundary, and C the Z-phases). Reproduced with permission of Elsevier from [41]

fact changing the peritectic reaction of $SmCo_5$ to an eutectic one [79]. The influence of Cu has been thoroughly investigated [61, 62]. The effect of Zr has been studied at fixed Cu and Sm contents [98]. A strong interaction between Sm and Zr is expected [91], although it is somehow accepted that Zr is substituting Co.

12.3 Coercivity Mechanism and the Development of High-Temperature 2:17-Type Magnets

12.3.1 The Sm(CoCu)$_5$ Cell Boundary Phase

The complex preparation process leads to the aforementioned heterogeneous nanostructure in the $Sm(Co_{bal}Fe_wCu_xZr_y)_z$ magnets. Subtle changes in microchemistry result in a system in which the domain wall energy ($\gamma = 4(K_1A)^{1/2}$) depends sensitively on the wall position and in which the walls remain pinned in regions where their energy is reduced. The gradient in Cu across the cell boundaries is facilitated by the presence of the Zr-rich lamellae and coincides with the gradient in the domain wall energy. This pinning-type coercivity mechanism is responsible for the high coercivities in these solid-state precipitation-hardened magnets.

Due to the large variety in heat treatment and compositional parameters an optimization of the $Sm(Co_{bal}Fe_wCu_xZr_y)_z$ magnets in terms of high-temperature magnetic properties is a complex task. Studies by J.F. Liu et al. [61–63] as well as C. Chen et al. [8] show that lower z values and higher amounts of Cu lead to a finer microstructure, which in turn results in a smaller temperature dependence of coercivity provided the appropriate Cu content is chosen. More specifically it was shown that for $z \sim 8.5$ and $x = 0.088$ a room temperature coercivity of $\mu_{0i}H_c = 4\,T$ was achieved, whereas for $z \sim 7$ and $x = 0.128$ a very high coercivity of 1.08 T at 500°C was obtained. Further work showed that increased Co content (lower Fe content) leads to maximum operation temperatures from 400 to 550°C. These magnets show a straight demagnetization curve (BH loop) in this temperature range, which is a requirement for dynamic applications [9]. Analytical electron microscopy across the Sm(CoCu)$_5$ cell boundary phase showed that the Cu content differs significantly from that of the matrix phase. It is also reported [58] that the anisotropy constant K_1 as well as the Curie temperature of this phase decreases dramatically with increasing Cu content as shown for K_1 in Fig. 12.5 and is finally lower than that of the 2:17-type matrix phase. Consequently, a transition from repulsive to attractive pinning could be expected with increasing Cu content. The pinning of domain walls has been related to the changes of K_1 during the complex annealing regime [43, 55, 102, 108, 109]. Another point of view is the consideration of the crystal structure of the cell boundary phase. Reports on the changes in phase equilibria and microstructure [15–20, 69] indicate that the cell boundary phase is actually composed of a mixture of 2:7 and 5:19-type phases, which are superlattices of the 1:5 phase, after annealing at 850°C, i.e., before the slow cooling ramp [15, 16]. The latter point has been reiterated by Goll et al. [35]. The intrinsic magnetic properties of the 2:7- and

5:19-type phases are not known and might differ somewhat from those of the 1:5 phase. However, most likely, they are in the range of those of the $Sm(Co_{1-x}Cu_x)_5$ system and thus one can expect finally very similar effects on the domain wall pinning behavior regardless of whether the changes are attributed to microchemical changes within or crystallographic variations of the cell boundary phase.

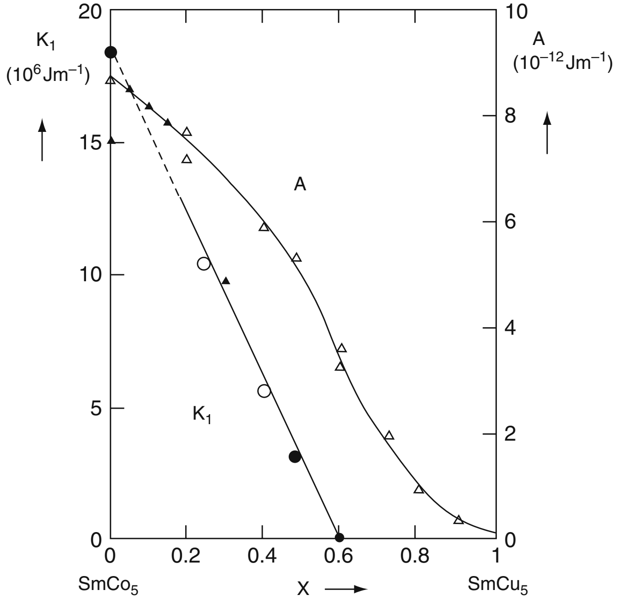

Fig. 12.5 Anisotropy constant K_1 at 300 K and exchange stiffness A of $Sm(Co_{1-x}Cu_x)_5$. K_1 shows a linear decrease with increasing Cu content. Reproduced with permission of American Institute of Physics from [58]

12.3.2 Alloy Optimization

Figure 12.6 shows the coercivity of $Sm(Co_{bal}Fe_wCu_xZr_y)_z$ samples as a function of z at room temperature, which were prepared by powder metallurgy production route [85], including jet milling, powder blending and compaction of oriented powder, and heat treatment (homogenization at 1,180–1,210°C, precipitation hardening at 800–860°C, and finally slow cooling to 400°C).

The coercivities of samples with the composition $Sm(Co_{bal}Fe_{0.144}Cu_{0.076}\,Zr_{0.022})_z$ show a narrow z-range with high coercivities, with a peak value above 3.87 T. With increased Zr, the maximum of coercivity is shifted to higher z values; a maximum coercivity of 4.4 T is found for $z = 8.35$. Even for $z > 8.5$ coercivities above 3.1 T were achieved. Zr is generally assumed to promote the desired microstructure for high coercivities. The compositions with higher Zr content were not single phase after homogenization. Some magnets contained considerable amounts of a Zr-rich

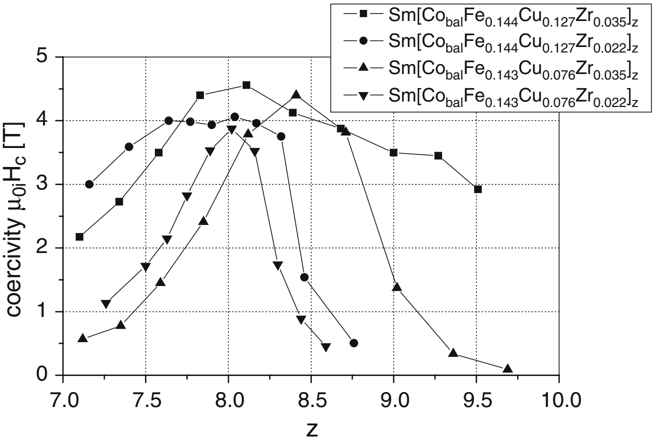

Fig. 12.6 Coercivity $\mu_{0i}H_c$ vs. z at room temperature. Reproduced with permission of Elsevier from [85]

phase, which was identified as $Zr_6(Co,Fe,Cu)_{23}$ with the Th_6Mn_{23} structure [67]. Nevertheless, these magnets had excellent coercivities and demagnetization curves with good squareness. The combination of higher Cu and higher Zr content leads to a very broad range of useful z values, with good coercivity (>2.7 T) up to $z = 9.5$. A higher Cu content considerably extends the useful range of z to lower z values, consistent with the results of Liu et al. [61, 62].

Figure 12.7 (left) shows the coercivity as a function of z for a selection of these compositions at 450°C. The highest coercivity is achieved with the compositions high in Cu. The influence of Cu is fairly well understood: the high coercivity in the Sm_2Co_{17}-type magnets is commonly attributed to the difference in magnetic properties between the $Sm_2(Co,Fe)_{17}$ matrix and the $Sm(Co,Cu)_5$ cell boundary phase [24, 25, 84, 93]. This difference is enhanced by an increasing Cu content in the

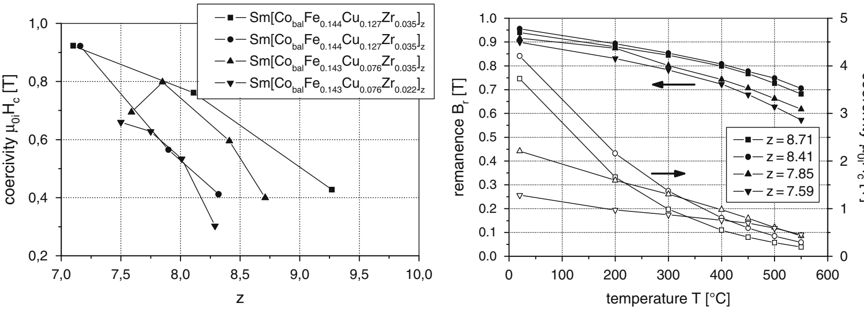

Fig. 12.7 Coercivity $\mu_{0i}H_c$ vs. z at 450°C (*left*); remanence B_r (*full symbols* → left axis) and coercivity $\mu_{0i}H_c$ (*empty symbols* → right axis) vs. temperature of $Sm(Co_{bal}Fe_{0.144}Cu_{0.076}Zr_{0.035})_z$ (*right*)

$Sm(Co,Cu)_5$ phase leading to a dramatic decrease of the anisotropy constant K_1 of this phase [58]. The maximum of the coercivity is shifted to lower z values, which are thus seen to lead to a better temperature coefficient of the intrinsic coercivity [63]. As an example, remanence and coercivity of $Sm(Co_{bal}Fe_{0.144}Cu_{0.076}Zr_{0.035})_z$ are shown in Fig. 12.7 (right) for the temperature range from room temperature to 550°C.

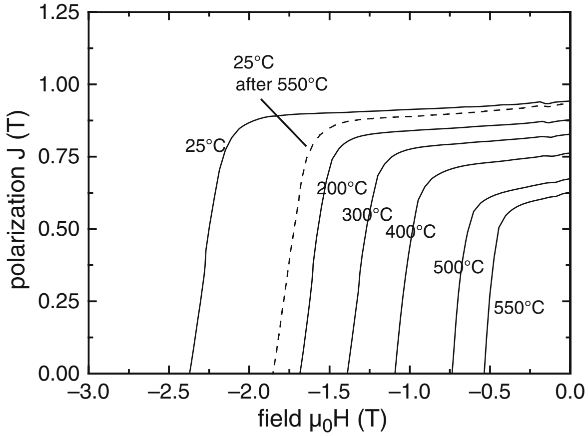

Fig. 12.8 Second quadrant demagnetization loops of $Sm(Co_{0.784}Fe_{0.1}Cu_{0.088}Zr_{0.028})_{7.19}$ for various temperatures. Reproduced with permission of Elsevier from [41]

The effect of compositional changes in $Sm(Co_{bal}Fe_vCu_yZr_x)_z$ alloys on the high-temperature magnetic properties has been studied systematically. A high level of both Cu and Zr is found to be effective for improving the high-temperature properties. The real benefit in compositions with high Cu content lays in the possibility to increase the Sm level and still achieve a high Cu concentration in the $Sm(Co,Cu)_5$ cell boundary phase. An increased Zr level shifts the optimum Sm content to lower levels, and magnets with excellent high-temperature coercivities were prepared with a samarium content well below the “2:17” stoichiometry. Figure 12.8 shows second quadrant demagnetization loops of $Sm(Co_{0.784}Fe_{0.100}Cu_{0.088}Zr_{0.028})_{7.19}$ for temperatures up to 550°C illustrating the excellent high-temperature properties ($(BH)_{max} = 82\,kJ/m^3$, $B_r = 0.67$ T, and $\mu_{0i}H_c = 0.74$ T) at 500°C [41].

SEM micrographs of the $Sm(Co_{0.784}Fe_{0.1}Cu_{0.088}Zr_{0.028})_{7.19}$-sintered magnet (Fig. 12.9) show a uniform cellular structure (the corresponding TEM bright field images are shown in Fig. 12.4). Figure 12.10 shows the STEM and HRTEM images of typical $Sm(Co_{0.784}Fe_{0.1}Cu_{0.088}Zr_{0.028})_{7.19}$ magnets (imaging plane perpendicular to the c-axis). The HRTEM image shows the 1:5 cell boundary phase with a width of about 5–10 nm. In the composition maps of Cu, Co, Fe, and Sm (Fig. 12.11), the bright regions represent a high concentration of the respective element and the dark regions are depleted in the element: the 2:17 matrix phase is rich in Co and Fe, while the cell boundary phase is rich in Cu and Sm.

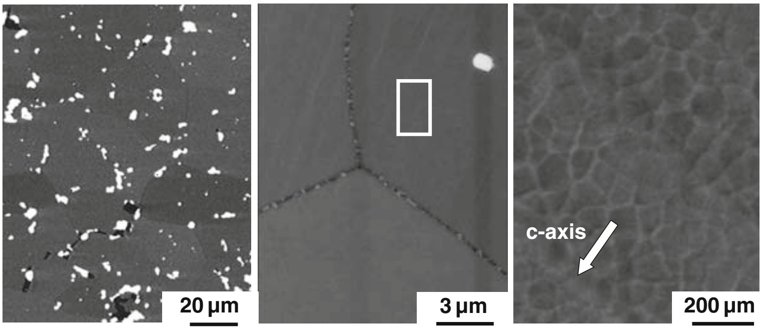

Fig. 12.9 Backscattered electron mode SEM images of a $Sm(Co_{0.784}Fe_{0.100}Cu_{0.088}Zr_{0.028})_{7.19}$-sintered magnet showing the coarse grain structure with some Sm-rich precipitates (*left*), a grain boundary with Zr-rich regions (*middle*) and (*right* – image taken within the area indicated by the frame in the *middle image*) the cellular network of 1:5-type phase and indications of the lamellar phase (c-axis approximately parallel to the imaging plane and perpendicular to the lamellar phase). Reproduced with permission of Elsevier from [41]

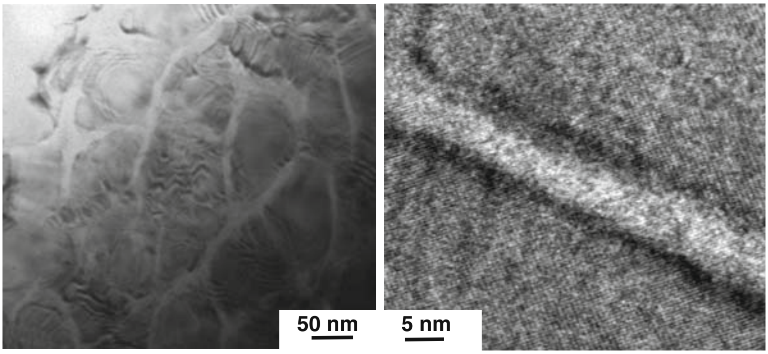

Fig. 12.10 STEM (*left*) image of a $Sm(Co_{0.784}Fe_{0.100}Cu_{0.088}Zr_{0.028})_{7.19}$ magnet (c-axis perpendicular to the imaging plane) and HRTEM (*right*) image showing the cellular phase in detail. Reproduced with permission of Elsevier from [41]

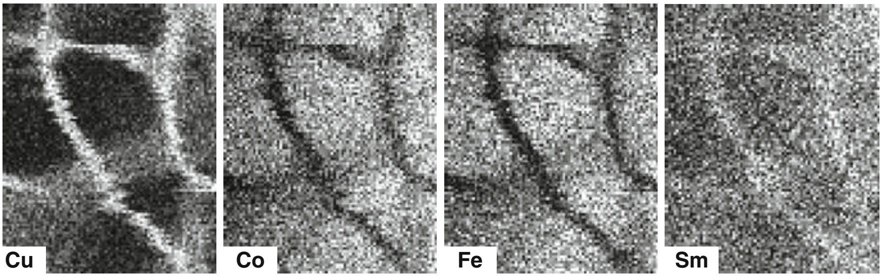

Fig. 12.11 Element mapping for Cu, Co, Fe, and Sm in a $Sm(Co_{0.784}Fe_{0.100}Cu_{0.088}Zr_{0.028})_{7.19}$ magnet (width of each image is 200 nm) confirming that the cell boundary phase is rich in Cu and Sm. Reproduced with permission of Elsevier from [41]

12.3.3 Stability at Operating Temperature

An important question is the stability of magnetic properties at operating temperatures exceeding 400°C. An analysis of the evolution of coercivity at room temperature after measurements at different temperatures shows that the coercivity of the magnets is decreased with increasing measurement temperature. A coercivity of up to 0.5 T was obtained at 550°C. No obvious change in the coercivity at room temperature is detected after high-temperature measurements below or at 400°C. However, the coercivity measured at RT starts to reduce after HT measurements above 400°C and the higher the measurement temperature, the larger the loss of coercivity at RT. After the measurement at 550°C, the coercivity at room temperature is reduced from 2.8 to 2.3 T [45]. The observed decrease in coercivity above 400°C was found to be due to microstructural changes in the bulk and not due to surface degradation. The losses in coercivity can be fully recovered when the last segment of the original heat treatment of the magnet (550–400°C with 0.7 K/min and 3 h at 400°C) is repeated (as shown in Fig. 12.12 (left)).

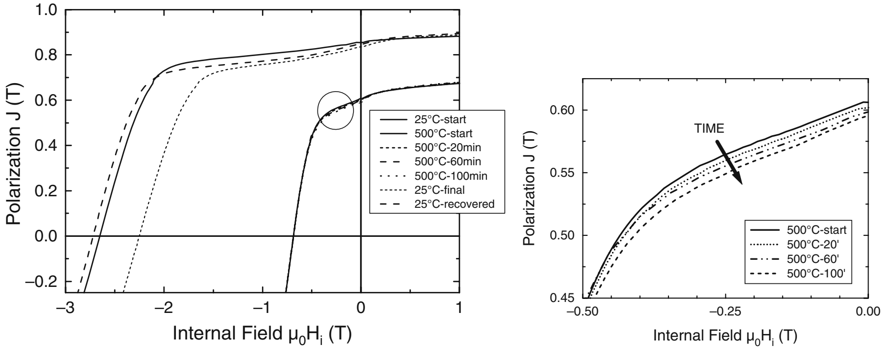

Fig. 12.12 Demagnetization curves of a Sm(Co$_{0.784}$Fe$_{0.100}$Cu$_{0.088}$Zr$_{0.028}$)$_{7.19}$-sintered magnet at RT (25°C – start), at 500°C after various time intervals, and again at RT after the high-temperature measurements (25°C – final) (*left*); enlargement of the circled area in the top figure showing the degradation of remanence during in situ high-temperature VSM measurements with increasing time (*right*). Reproduced with permission of IEEE Trans. Magn. from [45]

The exposure to temperatures as high as 550°C presents new challenges because of the reactions between the magnet and the environment. It has been demonstrated that exposure to air leads to a severe loss in the magnetic properties of the 2:17 SmCo magnets. Samples annealed in air form a surface region of about 20 μm thickness with enhanced oxygen content and a decreasing Sm content [45]. It was reported that the major cause for the magnetic loss is Sm depletion [10]. Sm is lost by vaporization from the surface, leaving an oxide of Fe–Co, and preventing the vaporization of Sm seems to be more challenging than preventing the surface oxidation. The Sm loss at the surface causes an increasing dip in the second quadrant demagnetization curve with increasing annealing time. Thus, surface protection by coating can minimize Sm depletion and is crucial for the application of the magnets at high temperature in air. The oxidation mechanism of high-temperature magnet grades has been examined in detail by Kardelky et al. [48].

12.4 Microchemistry and Pinning Behavior in Sm_2Co_{17}-Type Magnets

12.4.1 Redistribution of Cu and Slow Cooling

The temperature dependence of coercivity of the Sm_2Co_{17}-type magnets is determined by microstructure and microchemistry of the various phases. The cellular and lamellar phases are formed during isothermal aging but the coercivity after this stage is still low. Cu diffusion into the 1:5 cell boundary phase is assumed to take place during slow cooling and the higher the quenching temperature, the lower the Cu content in 1:5 phase [84]. The diffusion of Cu into the 1:5-type cell boundary phase leads to a modification of the magnetic properties of the 1:5-type phase and thus a significant domain wall energy difference between 2:17- and 1:5-type phases. Slow cooling is necessary to develop high coercivity at room temperature and the concomitant evolution of microchemistry of the phases in the Sm_2Co_{17}-type magnets needs to be understood in detail.

Figure 12.13 shows typical hysteresis loops of the $Sm(Co_{0.74}Fe_{0.1}Cu_{0.12}Zr_{0.04})_{7.5}$ ribbons subjected to aging at 850°C for 3 h without slow cooling or followed by slow cooling to different temperatures (600°C and 400°C). A coercivity of 3.0 T as well as strong domain wall pinning is observed at room temperature for the ribbons after aging at 850°C for 3 h and subsequent slow cooling to 400°C (type I), which is much higher than that of the ribbons without slow cooling (0.32 T); the latter sample is in the following referred to as type II. The coercivity of ribbons develops

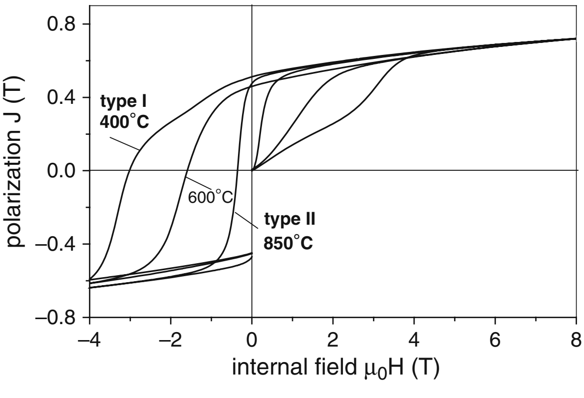

Fig. 12.13 Typical hysteresis loops of $Sm(Co_{0.74}Fe_{0.1}Cu_{0.12}Zr_{0.04})_{7.5}$ ribbons subjected to aging at 850°C for 3 h without slow cooling (type II) or followed by slow cooling to different temperature (600°C and 400°C (type I)). Reproduced with permission of American Institute of Physics from [108, 109]

mainly during slow cooling, very similar to the behavior observed in bulk and melt-spun Sm(Co,Fe,Cu,Zr)$_z$ materials subjected to a conventional precipitation-hardening regime.

Uniform cellular and lamellar structures are formed upon isothermal aging the as-spun ribbons at 850°C for 3 h, without subsequent slow cooling. The cell size is about 40 nm, which is smaller than that observed in the conventional sintered Sm(Co,Fe,Cu,Zr)$_z$ magnets [27, 28]. After slow cooling no obvious changes in cell size and density of lamellar phase are observed [105, 107].

Thus, the evaluation of coercivity should be attributed to chemical modifications of the cell boundary phase, especially of the Cu distribution. Nanoprobe energy dispersive X-ray analysis (EDX) profiles of Cu in the vicinity of a matrix/cell boundary phase in the type I and type II samples (Fig. 12.14) show that the 1:5 cell boundary phases are enriched in Cu, in contrast to the 2:17 matrix phase, but the Cu distribution in the cell boundary phase varies significantly in the type I and type II samples: a large gradient of the Cu content is observed in the cell boundary phase of the type I sample. The Cu content in the middle of the cell boundary phase (24 at.%) is three times as high as that of the region near the 2:17 phase, similar to that observed in bulk and melt-spun Sm(Co,Fe,Cu,Zr)$_z$ materials subjected to conventional magnetic hardening [33, 43]. However, the Cu content in the cell boundary phase of the type II sample is more uniform, revealing the redistribution of Cu within the cell boundary

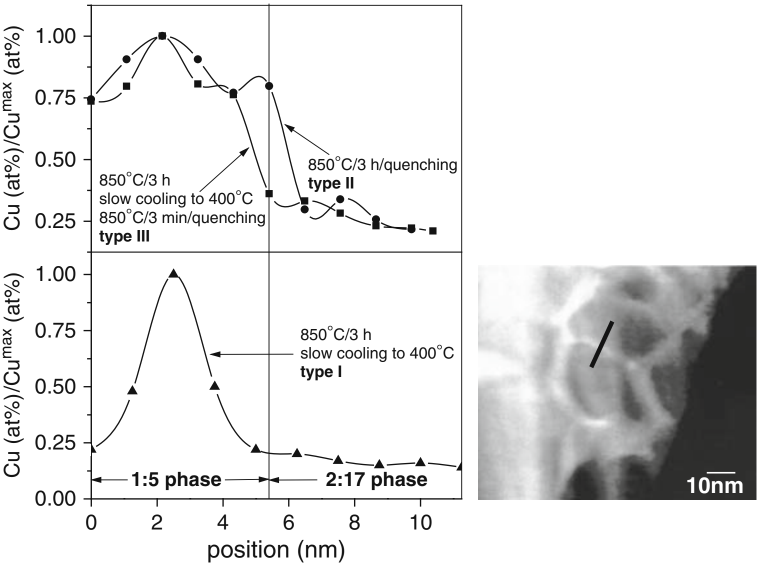

Fig. 12.14 EDX line scans (marked as a *black line* in the STEM image) for Cu across a matrix/cell boundary interface in Sm(Co$_{0.74}$Fe$_{0.1}$Cu$_{0.12}$Zr$_{0.04}$)$_{7.5}$ ribbons, which have been aged at 850°C for 3 h and (1) slow cooled to 400°C and quenched (*bottom* – type I), (2) quenched from 850°C without slow cooling (*top* – type II), and (3) slow cooled to 400°C and quenched, then rapidly reheated to 850°C and quenched after a 5 min dwell (*top* – type III). Reproduced with permission of American Institute of Physics from [108, 109]

phase during slow cooling. An obvious difference of the chemical composition is not observed in the 2:17 matrix phase of the type I and type II samples (these results are consistent with three-dimensional atom probe (3DAP) analysis [36]). The solubility of Cu in 2:17 SmCo phase is 16 at.% at 1,200°C, which is significantly reduced to 4 at.% at 800°C [79]. Thus, most of the Cu atoms in the ribbons should already segregate in the 1:5 cell boundary phase during isothermal aging due to the very low solubility of Cu in the 2:17 matrix phase at that temperature, and the amount of Cu diffusing into the cell boundary phase during slow cooling should be quite limited.

The coercive force of $Sm(Co,Cu)_5$ alloys can be significantly increased by aging at low temperature due to the occurrence of a spinodal decomposition [72]. Hofer [46] reported an ideal mixing of Co and Cu in the 1:5 composition at high temperature ($>800°C$) and a separation into a $SmCo_5$ phase containing some Cu in solution and a Co-modified $SmCu_5$ phase due to a spinodal-type decomposition at low temperature. The annealing temperature, time, and cooling rate are of great importance because the resulting properties of $Sm(Co,Cu)_5$ alloy are very structure dependent. It could be argued that it is a kind of decomposition-type reaction taking place in the Cu-rich $Sm(Co,Cu)_5$ cell boundary phase of 2:17 SmCo magnets during slow cooling, leading to a large gradient of the Cu content within this phase. On the other hand, the formation of the gradient could also help to reduce lattice strain between the cell and the boundary phases.

Magnetic viscosity $S = -\mathrm{d}M/\mathrm{d}\ln t$ (with M the magnetization of the samples and t the time) measurements in the two types of $Sm_2(Co,Fe,Cu,Zr)_{17}$ ribbons have been used to deduce the activation volume v_a and its temperature dependence, in relation to that of the coercive field [40]. A clear difference in the $v_a(T)$ between the two types of ribbons, consistent with differences in $H_c(T)$, has been found. At room temperature the type I ribbon has a high coercivity, ${}_iH_c$, in contrast to the relatively low coercivity of type II. In type II ${}_iH_c$ and H_c almost coincide in the whole range of T and their T dependence is related linearly to that of $v_a{}^{-2/3}$. According to the "Global model" of coercivity and magnetic viscosity [2, 31, 32] such a behavior is expected for materials in which (i) the critical elementary magnetization reversal processes (CEMRPs) are mainly governed by the intrinsic properties of the magnetic main phase of the material and (ii) second-order anisotropy is dominant. These CEMRPs are assumed to be concentrated in small critical volumes of typical size v_a, as derived from viscosity data. In Sm_2Co_{17}-type magnets, the CEMRPs are domain wall unpinning events. The difference in ${}_iH_c$ and H_c and the stronger T dependence of $v_a{}^{-2/3}$ in the type I material can naturally be related to the more complicated chemical microstructure of this sample, in particular, the large Cu concentration gradient in the 1:5 cell boundary phase. Here the CEMRPs are not simply related to the intrinsic properties of the main phase (thus v_a depends not only on main phase properties). ${}_iH_c$ of type I decreases monotonically with increasing T whereas that of type II becomes almost constant when approaching RT. This is attributed to the different Cu concentration gradients in the 1:5 cell boundary phase in the two types of ribbon. In the same manner, the positive T coefficient of coercivity between 473 and 773 K (compare Fig. 12.18) for type II can be explained. The large differences in the $v_a(T)$ of the two types of ribbons are consistent with their $H_c(T)$ behavior. The activation length $l_a = {v_a}^{1/3}$ of type I decreases from 7.8 nm at room temperature to 2.4 nm at 20 K, whereas that of type II decreases from 12.1 nm at room temperature to 3.7 nm at 4 K. The typical width of the 1:5 cell boundary phase in the ribbons is ~7 nm, which roughly agrees with the room temperature domain wall width δ_w of the main phase.

The coercive field of a 180° domain wall can be approximated by [55] ${}_iH_c = 1/(2\,J_s \cos\psi_0) \times (\mathrm{d}\gamma\,(z)/\mathrm{d}z\,)_{\max} - N_{\mathrm{eff}}M_s$ (J_s: spontaneous polarization; ψ_0: angle between applied field and the easy direction; $(\mathrm{d}\gamma(z)/\mathrm{d}z)_{\max}$: maximum slope of the wall energy in the phase boundary; the term $N_{\mathrm{eff}}M_s$ describes the force of a locally acting effective demagnetizing field). A homogeneous Cu content thus leads to a low gradient of the domain wall energy $(\mathrm{d}\gamma(z)/\mathrm{d}z)_{\max}$ in the sample without slow cooling and thus weak domain wall pinning and low coercivity. In contrast, the larger gradient of the Cu content in the cell boundary phase after slow cooling yields stronger domain wall pinning within the cell boundary phase, resulting in high coercivities. The main contribution of slow cooling to the coercivity of 2:17 SmCo magnets is the development of a large Cu gradient within the Cu-rich Sm(Co,Cu)$_5$ cell boundary phase. The significant improvement in the coercivity of 2:17 SmCo magnets could result from the large gradient of domain wall energy within the Cu-rich Sm(Co,Cu)$_5$ cell boundary phase and not from the Cu diffusion from the 2:17 phase to the 1:5 phase, as proposed by the well-known two-phase domain wall pinning model, the latter being based on a uniform Cu content and domain wall energy in the cell boundary phase [22, 24, 25, 27, 28, 34, 43, 66].

12.4.2 Stability of Microchemistry

The stability of microchemistry in Sm(Co,Fe,Cu,Zr)$_z$ magnets at high temperature and its effect on the magnetic properties need to be addressed. Figure 12.15 shows that an additional aging at 850°C for only 5 min, after having completed the slow cooling regime, has a dramatic effect on the magnetic properties. Figure 12.16(a) shows the dependence of the coercivity of the ribbons upon aging temperature for an additional 5 min annealing in more detail. A higher aging temperature leads to higher losses in the coercivity, and the ribbons subjected to only 5 min aging at 850°C (type III) show a very low coercivity of 0.16 T, which is only 5% of the value of the original ribbon (type I). Further changes in coercivity are not observed with further increasing aging time at 850°C, i.e., all the changes took place within the initial 5 min (Fig. 12.16(b)).

Figure 12.14 shows also the nanoprobe EDX profile of Cu obtained by a line scan across the interface between the 2:17 matrix and the 1:5 cell boundary phase in the type III sample. After an additional 5 min aging at 850°C (type III), no obvious change of chemical composition is observed in the 2:17 matrix phase, but the Cu distribution within the cell boundary phase becomes again more homogeneous and the large gradient of the Cu content is no longer detectable. A rapid redistribution of Cu within the cell boundary phase has taken place and is very similar to that

Fig. 12.15 Hysteresis loops of ribbons before (type I) and after (type III) additional aging at 850°C for 5 min. Reproduced with permission of American Institute of Physics from [108, 109]

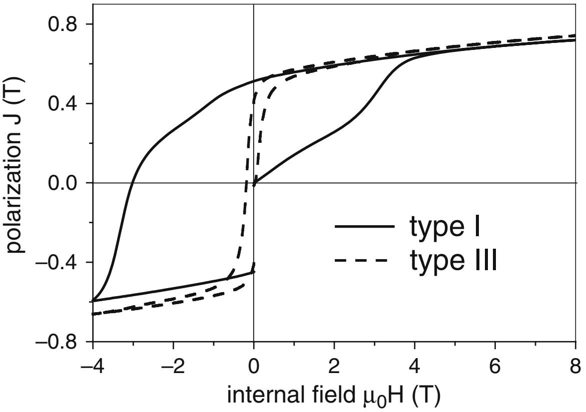

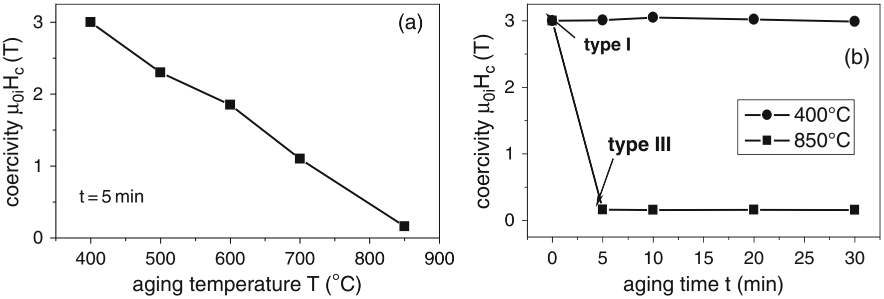

Fig. 12.16 Dependence of the coercivity of $Sm(Co_{0.74}Fe_{0.1}Cu_{0.12}Zr_{0.04})_{7.5}$ ribbons on (**a**) aging temperature *T* (additional isothermal aging for 5 min after having completed the slow cooling regime) and (**b**) aging time *t* (for isothermal aging at 850 and 400°C). Reproduced with permission of American Institute of Physics from [108, 109]

observed in the ribbons subjected to isothermal aging at 850°C for 3 h without slow cooling (type II).

It is generally accepted that a high Cu content in the cell boundary is beneficial for the development of high coercivity in $Sm(Co,Fe,Cu,Zr)_z$ magnets both at room temperature and at high temperatures since more Cu in the 1:5 boundary phase leads to a lower domain wall energy of the 1:5 cell boundary phase and a larger domain wall energy difference, assuming that the anisotropy of the 2:17 matrix phase does not change. According to this well-known two-phase domain wall pinning model, the dramatic loss of the coercivity in the type II sample can be attributed to the significant reduction of the Cu content in the 1:5 cell boundary phase, and Cu should diffuse into the 2:17 matrix phase during the subsequent short-time aging. However, the above EDX shows that the Cu content in the 2:17 matrix phase remains more or less constant after the short aging. In fact, the solubility of Cu in the 1:5 phase is much higher than that in the 2:17 matrix phase and a complete solubility is expected between $SmCo_5$ and $SmCu_5$ only above 800°C [79]. Thus, most of the Cu should already segregate in the 1:5 cell boundary phase during isothermal aging due to the very low solubility of Cu in the 2:17 matrix phase at this temperature, and the amount of Cu diffusing into the cell boundary phase during slow cooling should be quite limited. Moreover, a short time such as 5 min seems not to be sufficient for a significant diffusion of Cu from the 1:5 phase into the 2:17 phase to take place. Thus, Cu appears to be present in the 1:5 cell boundary phase after the additional aging at 850°C for only 5 min, and a redistribution of atoms (Sm,Co,Cu,Fe,Zr) within the very thin cell boundary phase (width around 5–10 nm) appears to be more likely.

Based on the Cu content dependence of the anisotropy constant K_1 as well as the domain wall energy γ for Cu-substituted Sm(Co,Cu)$_5$ alloys [58], simplistic γ profiles across the 1:5 cell boundary phase for samples of type I and II can be derived. In the case of a high-coercivity state (type I), a strong pinning occurs within the cell boundary phase due to the very large slope of the domain wall energy. For a thickness of the cell boundary phase larger than that of the domain wall, the domain wall may be attractively pinned at the center of the cell boundary phase, due to the lower domain wall energy of these Cu-rich regions. In addition, the redistribution of Cu within the 1:5 cell boundary phase during slow cooling leads to a significant reduction in Cu content in the 1:5 phase close to the interface to the 2:17 matrix phase. Thus, due to the irregularity of the domain wall energy at this interface the pinning mechanism might be even more complex after slow cooling. The 2:17 domain walls may be repelled at this interface by a Cu-deficient 1:5 phase with higher domain wall energy (repulsive pinning). However, when the size of the inhomogeneities, i.e., the thickness of the 1:5 cell boundary phase, is comparable to or smaller than the domain wall thickness, $\delta_{\mathrm{w}} \approx 5\,\mathrm{nm}$, the characterization of the pinning is more complicated.

Further, temperature-dependent changes of the domain wall energy γ profile across the 1:5 cell boundary phase need to be considered. For the ribbons without slow cooling, the EDX analysis shows that the Cu distribution within the 1:5 cell boundary phase is roughly uniform. The coercivity at low or room temperature is caused by a repulsive pinning at the cell boundaries and the complicated temperature dependence of the coercivity can still be explained by the conventional repulsive/attractive model, i.e., a crossover between repulsive and attractive pinning at a certain temperature T. When the sample is slowly cooled to lower temperatures, the Cu distribution within 1:5 phase becomes inhomogeneous and a large gradient of Cu content and domain wall energy is formed, leading to a significant improvement of the coercivity at room temperature. It can be assumed that the Cu-rich 1:5 layer in the middle of the cell boundary becomes paramagnetic at a certain temperature, depending on the amount of Cu. The higher the measuring temperature, the more the fraction of paramagnetic 1:5 phase. In this case, coercivity may be controlled by a competition between domain wall pinning at the magnetic Cu-poor 1:5 layer near the 2:17 cell and nucleation of reversed domains in the ferromagnetic 1:5 layers or 2:17 cells. When the measuring temperature is further increased, all of the 1:5 phase becomes paramagnetic and the coercivity could be related to nucleation of reversed domains in the ferromagnetic 2:17 cells.

Another point to be considered, apart from microchemical modifications, is the possibility that the cell boundary phase is actually composed of a mixture of 2:7- and

5:19-type phases after annealing at 850°C, i.e., before slow cooling [15, 16]. This scenario cannot be excluded and this might well affect the above-mentioned differences in domain wall energy between matrix and cell boundary phases [35]; however, it is difficult to imagine that these crystal structure changes are also reversible as demonstrated for the microchemical changes. In any case, these considerations illuminate that the magnetic and microchemical properties of the $\mathrm{Sm(Co,Cu)_5}$-type cell boundary phase, corresponding in fact to the oldest rare earth–transition metal magnet (compare, for example, "Giant intrinsic magnetic hardness in $\mathrm{SmCo_{5-x}Cu_x}$" as reported by Oesterreicher et al. [73] or Kerschl et al. [51]), deserve more attention and a full understanding of the magnetic, structural, and microchemical properties of the cell boundary phase during slow cooling is indispensable for clarifying the very complex coercivity mechanism of 2:17 SmCo magnets.

12.4.3 "Anomalous" Coercivity Behavior

The quenching temperature dependence of coercivity at room temperature and the temperature stability of $\mathrm{Sm(Co_{0.74}Fe_{0.1}Cu_{0.12}Zr_{0.04})_{7.5}}$ ribbons are shown in Fig. 12.17. The coercivity at room temperature continues to decrease with increasing quenching temperature and is reduced to only 0.32 T for the ribbons after aging at 850°C for 3 h without slow cooling, revealing that the coercivity at room temperature develops mainly during slow cooling. The temperature coefficient of the coercivity is negative over the entire temperature range (RT −500°C) for the ribbons quenched at 750°C and below. In contrast, a higher quenching temperature leads to a lower coercivity at room temperature but a smaller temperature coefficient and even a positive one (200–500°C), the last phenomenon also called an "anomalous" coercivity behavior. Coercivities of 0.22 T at 200°C and 0.32 T at 500°C are obtained in the ribbons aged at 850°C for 3 h without slow cooling, similar to those observed in bulk and melt-spun $\mathrm{Sm(Co,Fe,Cu,Zr)_z}$ magnets with very low Cu content subjected to the conventional aging program [33, 61, 62, 80, 113].

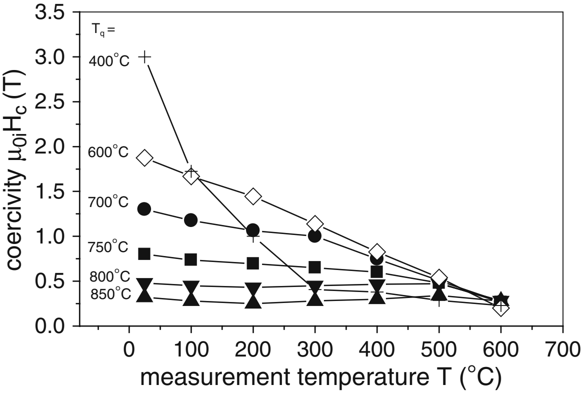

Fig. 12.17 Coercivity vs. measurement temperature of $\mathrm{Sm(Co_{0.74}Fe_{0.1}Cu_{0.12}Zr_{0.04})_{7.5}}$ ribbons (3 h at 850°C, then slow cooling to temperature T_q (as indicated on the *left*), followed by quenching). Reproduced with permission of IEEE Trans. Magn. from [104–107]

Figure 12.18 (left) shows the coercivity vs. measurement temperature of the ribbons quenched from 850 and 800°C indicating a complex coercivity behavior upon changing temperature with three distinguished regions for the domain wall energy γ: the transition from I – repulsive pinning with $\gamma_{2:17} < \gamma_{1:5}$ to II – attractive pinning with $\gamma_{2:17} > \gamma_{1:5}$. Furthermore, one can assume a nucleation-type mechanism (III) to be active in a comparatively narrow temperature window (III) between the Curie temperature of the 1:5 cell boundary phase and that of the 2:17 matrix phase. These findings are consistent with results by Tang et al. [99]. At the crossover from region II to III, one can assume that the 2:17 cells become magnetically isolated, provided the thickness of the cell boundary phase is sufficient to assure magnetic decoupling (compare Skomski et al. [89] for an evaluation of exchange through non-magnetic insulating matrix), and the CEMRPs are governed by nucleation in the cell interior. At this point, i.e., above $T_C(1{:}5)$, one should also expect a drastic deviation from the phenomenological relationship $v_a \sim \delta_w{}^3$ [30], and this has actually been shown by Panagiotopoulos et al. [75]. The temperature coefficient of coercivity (Fig. 12.19 (right)) becomes negative when the ribbons are cooled below 750°C and the lower the quenching temperature, the more negative the temperature coefficient of coercivity. A coercivity of 0.53 T at 500°C was obtained in the sample quenched at 600°C.

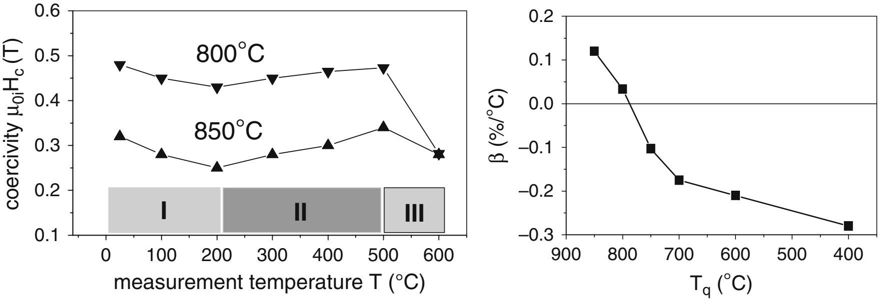

Fig. 12.18 Coercivity vs. measurement temperature of $Sm(Co_{0.74}Fe_{0.1}Cu_{0.12}Zr_{0.04})_{7.5}$ ribbons quenched from 850 and 800°C indicating an unconventional coercivity behavior with temperature: the transition from I – repulsive pinning with $\gamma_{2:17} < \gamma_{1:5}$ to II – attractive pinning with $\gamma_{2:17} < \gamma_{1:5}$ and III – nucleation type with $T > T_C(1{:}5)$ (*left*). Temperature coefficient of intrinsic coercivity β (200–500°C) vs. quenching temperature T_q (*right*). Reproduced with permission of IEEE Trans. Magn. from [104–107]

The Cu content in the 1:5 cell boundary phase can be controlled by the quenching temperature and thus the coercivity and its temperature coefficient are affected strongly not only by the alloy composition but also by the aging program. A low Cu content in the 1:5 cell boundary phase is helpful to develop positive temperature coefficients [33, 61, 62, 113]. A positive temperature coefficient of coercivity as well as a negative one can be obtained even in $Sm(Co,Fe,Cu,Zr)_z$ ribbons with a quite high Cu content by quenching from high temperature. On the other hand, a lower quenching temperature leads to a more negative temperature coefficient of the coercivity.

12.5 Magnetic Domains and Coercivity

12.5.1 Analysis of Magnetic Microstructure

The analysis of the magnetic microstructure in these complex multiphase nanostructures can further the understanding of the evolution of coercivity during the slow cooling ramp (usually around 0.7 K/min). Lorentz microscopy on thinned specimen reveals a zigzag-shaped domain pattern, which follows the cell boundaries [27, 28, 43, 112]. This observation is consistent with the domain walls being pinned at the cell boundaries of the prismatic cellular microstructure and based on the intrinsic magnetic properties of the various phases present (the anisotropy constant K_1 of the cell matrix is about 2.6 times larger than that of the cell boundary phase whereas the exchange constant A can be assumed to be comparable [93]). It can be assumed that this interaction is of attractive type at room temperature. It should be noted, however, that domain observation by TEM has only limited relevance concerning the domain structures of bulk materials and the change of those structures in a magnetization process because domain structures are very sensitive to the sample thickness [47], and therefore, the domains in samples thinned for TEM investigation can be very different from those in the bulk. Some early work using magneto-optic Kerr microscopy reports an irregular laminar domain structure [54, 23, 24, 25, 65] and that reverse domains originate at grain boundaries [60].

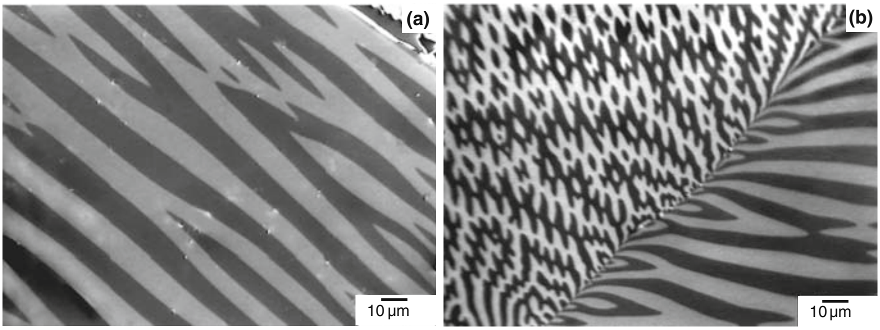

Fig. 12.19 Kerr microscopy images taken in a coarse-grained and homogeneous region of the Sm_2Co_{17} as-cast alloy. (**a**) Wide domains separated by 180° domain walls on the surface of a grain with its magnetically easy axis (c-axis) almost parallel to the imaging plane – "well-oriented grain"; (**b**) domain structures of a misoriented grain (*left*) and a well-oriented grain (*right*). At the grain boundary, the latter shows the effect of two-phase domain branching on its boundary perpendicular to the easy axis. Reproduced with permission of Elsevier from [41]

Figure 12.19 shows Kerr microscopy images of as-cast Sm_2Co_{17}; a domain structure typical for single-phase bulk high-anisotropy easy-axis-type ferromagnets is observed [47, 64]. The domain structure on the surface of such polycrystalline samples depends on the intrinsic magnetic properties of the material, in particular the spontaneous polarization J_s, the exchange stiffness A, and the anisotropy constants, most importantly K_1. But it also depends on the size (thickness) of the grains as well as the orientation of the grain surface with respect to the magnetically easy axis. Domains separated by 180° domain walls on a weakly misoriented surface of a grain (i.e., the easy axis is almost parallel to the imaging plane) can be seen in Fig. 12.19(a). Domain patterns on a strongly misoriented surface are shown in Fig. 12.19(b – top part), and so-called two-phase domain branching at the boundary of a well-oriented grain is shown in Fig. 12.19(b – bottom part).

12.5.2 Domains and Processing Parameters

The aforementioned high-temperature grades of sintered SmCo 2:17-type magnets have been cooled slowly from the aging temperature of 850°C to different temperatures T_q and then quenched. The $Sm(Co_{0.784}Fe_{0.1}Cu_{0.088}Zr_{0.028})_{7.19}$ magnet slowly cooled to 400°C develops the coercivity fully, whereas magnets quenched from $T_q =$ 750°C or higher show very small or almost no coercivity. A relatively sharp increase in coercivity can be observed around $T_q = 725°C$ (Fig. 12.20).

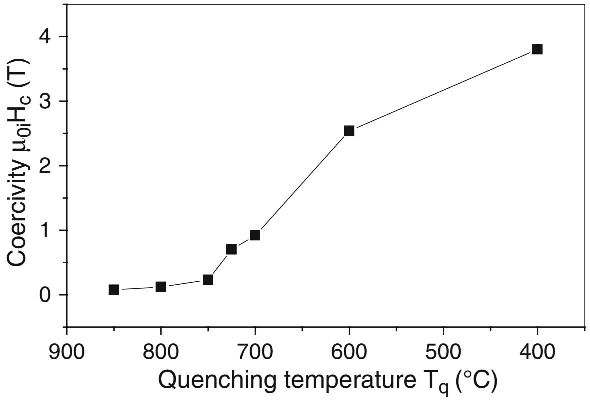

Fig. 12.20 Evolution of coercivity at room temperature in dependence on quenching temperature T_q from the slow cooling ramp of $Sm(Co_{0.784}Fe_{0.100}Cu_{0.088}Zr_{0.028})_{7.19}$-sintered magnets

Figure 12.21 shows the magnetic domain structure observed by Kerr microscopy and magnetic force microscopy (MFM) of thermally demagnetized magnets, which have been annealed at 850°C and quenched, or slowly cooled from 850°C to $T_q =$ 800 − 750 − 700 − 600 − 400°C and then quenched. The nominal c-axis is in all cases perpendicular to the imaging plane. The magnets quenched from $T_q \geq 750°C$ show very coarse domain structures. According to Fig. 12.20 the coercivity of these three magnets is very small. A comparison of these coarse structures in the upper two rows of Fig. 12.21 with those in the lower row shows that MFM and Kerr microscopy yield the same results if the characteristic lengths of the investigated magnetic structure are larger than the optical resolution limit of about 300 nm.

The magnet slowly cooled to 400°C, thus exhibiting maximum coercivity, and shows a very fine magnetic domain contrast, hardly resolved by Kerr microscopy. As MFM senses here only the vertical components of the force gradient of the magnetic stray field, all regions (here cells) that have the same magnetization direction

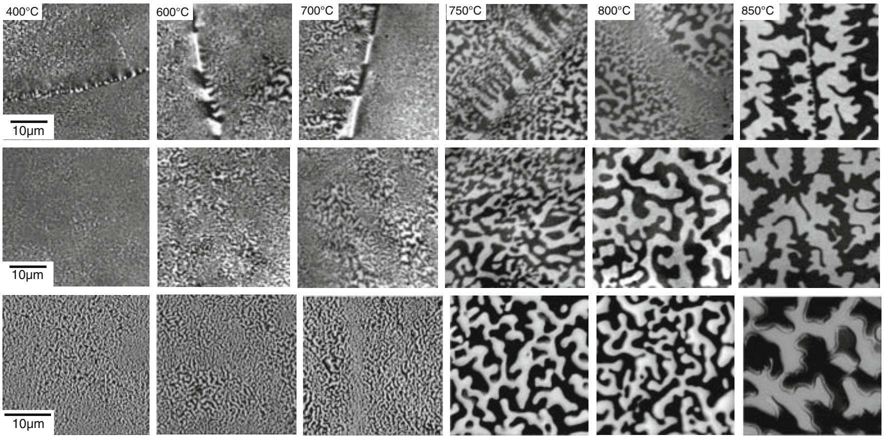

Fig. 12.21 Domain structure observed by Kerr microscopy (*two top rows*) and MFM (*bottom row*) of thermally demagnetized high-temperature grade $Sm(Co_{0.784}Fe_{0.100}Cu_{0.088}Zr_{0.028})_{7.19}$ magnets (nominal c-axis is perpendicular to the imaging plane) quenched from different temperatures (as indicated in the *bottom row images*) on the slow cooling ramp. The Kerr images of the *first row* show clearly that the grain boundary also has a very specific magnetic contrast. Reproduced with permission of Elsevier from [41]

will constitute a single feature in the magnetic contrast. The high-resolution MFM images in Fig. 12.22 (left: scan size of 10 μm × 10 μm) with the nominal c-axis perpendicular (a) and parallel (b) to the imaging plane clarify that the areas of uniform magnetic contrast extend over several dozens of individual cells. The overall morphology of the cellular structure with cell sizes of about 100 nm and the overlying Zr-rich lamellar phase within grains of several tens of microns are comparable for all of these magnets, regardless of the quenching temperature T_q.

In the whole range of considered quenching temperatures T_q and, consequently, in the whole range of ${}_iH_c$, the magnetic domain structure is considerably coarser than the cellular structure. Nevertheless, the physical nature of the domains in the left and in the right parts in Fig. 12.21 is obviously different. For the samples cooled from $T_q \geq 750°C$ the differences in the intrinsic magnetic properties (in particular in the anisotropy constant K_1) of the 2:17R-type cells and the 1:5-type cell boundary phase are relatively small. Thus, because the cells as well as the cell boundaries are coherent to each other within the large grains, the latter can be considered as single crystals with weakly fluctuating intrinsic magnetic properties. As a first approximation, the coarse domain structure is associated with effectively homogeneous intrinsic magnetic properties close to those of the 2:17R phase. Therefore, as expected, the domain structure of Fig. 12.23 is similar to that of coarse-grained 2:17R material, shown in Fig. 12.19(a), which does not have a cellular microstructure and Z-phase lamellae. In the case of Fig. 12.23, however, the cellular microstructure and the Z-phase are present, but no influence of them on the magnetic microstructure can be recognized.

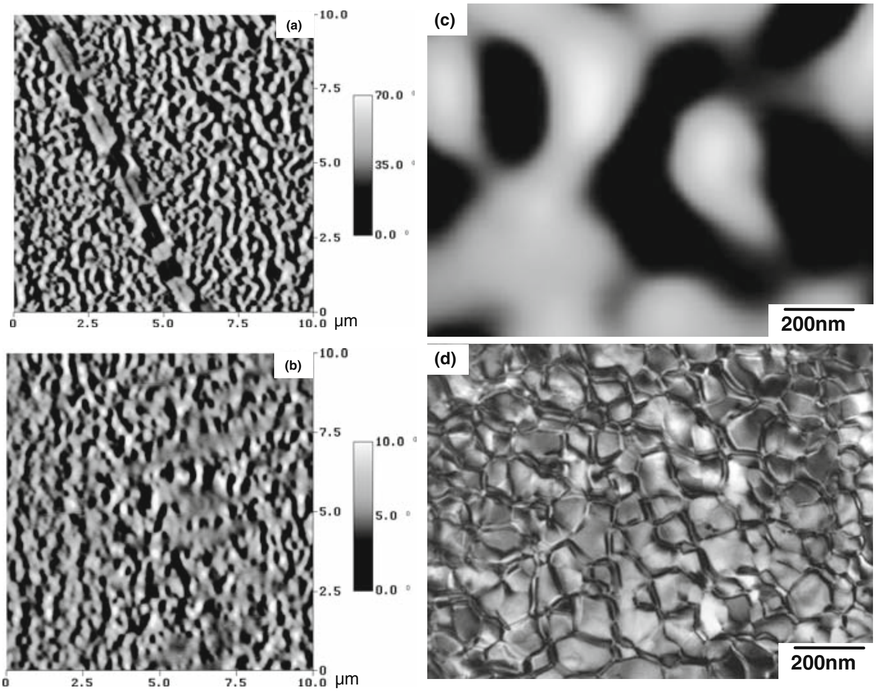

Fig. 12.22 Domain structure observed by MFM of thermally demagnetized $Sm(Co_{0.784}Fe_{0.100}Cu_{0.088}Zr_{0.028})_{7.19}$ magnets (slow cooled to 400°C, i.e., in the high-coercivity state): (**a**) nominal c-axis perpendicular to the imaging plane showing also a distinct magnetic contrast in the grain boundary phase and (**b**) nominal c-axis parallel to the imaging plane showing some strip-like features, which could be attributed to the lamellar phase. The large difference in the phase shift could be consistent with the difference in the stray field along the easy and hard directions of magnetization (*left*). Magnetic domain structure observed by MFM (**c**) and microstructure observed by TEM (**d**). The MFM image has been digitally enlarged to match the magnification of the TEM image (*right*) (nominal c-axis is in both cases perpendicular to the imaging plane; not the same area)

On the other hand, in optimized, i.e., slowly cooled to 400°C, magnets the high gradient in the Cu concentration in the 1:5 cell boundary phase will give rise to large fluctuations in the intrinsic properties of this phase. In particular, K_1 and the spontaneous magnetization M_s will be considerably smaller in the cell boundary regions than in the 2:17R-type cells. Therefore, the domain structures in Fig. 12.22 and in the left part of Fig. 12.21 may be considered as cooperative phenomena similar and akin to interaction domains [13] well known for fine-grained ferromagnetic materials where the interaction between the small grains is predominantly of magnetostatic nature [47, 53]. In the highly coercive materials considered here, the magnetic interaction between the 2:17R cells is not purely magnetostatic but the exchange interaction between the cells is expected to be much smaller compared to the exchange interaction within the cells and to the exchange coupling between the cells of the low-coercivity samples of the right part of Fig. 12.21.

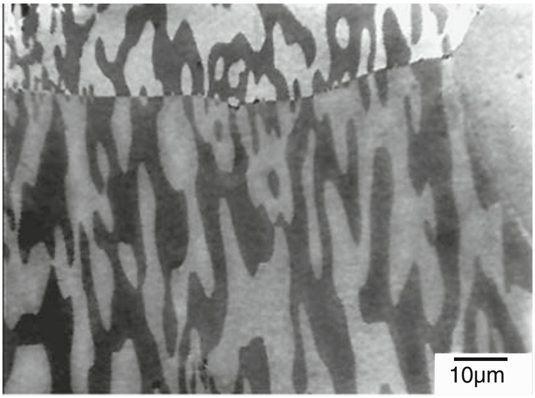

Fig. 12.23 Kerr microscopy image of $Sm(Co_{0.784}Fe_{0.100}Cu_{0.088}Zr_{0.028})_{7.19}$ quenched from 850°C (corresponding to the *right column* of Fig. 12.21) with the nominal c-axis parallel to the imaging plane

Subtle microchemical changes [108, 109], mainly the change of the concentration and distribution of Cu in the cell boundary phase, occurring in the slow cooling ramp, can explain the hysteresis phenomena observed. The cell boundaries are usually considered as pinning centers for domain walls. To a lesser extent, interface deformation strains due to the lattice misfit between the different phases that increases during the slow cooling may also enhance the strength of pinning [66]. Xiong et al. [102] reported that the composition of the Z-phase is also affected by the slow cooling treatment, more specifically they observed that zirconium replaces samarium to form $Zr(Co,Fe)_3$ at this processing stage. This in turn might have implications with regard to the domain wall energy of the Z-phase and thus also might be of relevance when considering local wall energy minima acting as pinning sites for the domain wall movement [49, 50, 87].

However, the concept of domain walls (to be pinned) is to some degree questionable in the case of the high-coercivity magnets. Classic domain walls are thin transition regions between homogenously magnetized domains that can be well determined by methods of micromagnetism [47]. In the magnetic microstructure of Fig. 12.22, the walls are expected to be quite different from classic domain walls and the exact pinning mechanism still has to be elucidated. In ideal interaction domains, the elementary magnetic units are single-domain particles, which would correspond here to the uniformly magnetized 2:17R cells. Consequently, the boundaries of the interaction-domain-like structures in Fig. 12.22 could coincide with boundaries of 2:17R cells, similar as the zigzag-shaped patterns observed in thinned samples, by using Lorentz-mode TEM.

The nature of the magnetic domain structure (in particular the domain width) is very sensitive to details of the processing procedure, which is needed to attain high coercivity. In high-temperature $Sm(Co_{0.784}Fe_{0.1}Cu_{0.088}Zr_{0.028})_{7.19}$ magnets, the typical domain width is less than 1 μm, but significantly larger than the typical size of 2:17R phase cells of about 100 nm, the latter surrounded by the 1:5 cell boundary phase. On the other hand, if such a magnet is quenched straight from the aging temperature, i.e., the slow cooling ramp is omitted, the resulting domain structure is much coarser (domain width $\sim$10 μm) and the coercivity is small ($<$0.1 T), although no significant changes in the microstructure occur during slow cooling (only subtle microchemical changes take place within and near the 1:5 cell boundary phase).

12.6 Non-equilibrium Processing Routes

Due to their large magnetocrystalline anisotropy $SmCo_5$ and Sm_2Co_{17} compounds are prototypical candidates for developing coercivity through a decrease of grain sizes. Non-equilibrium processing routes such as melt spinning [33], mechanical alloying [1, 21, 86, 97, 101, 114], or reactive milling [38, 56] as a variation of the hydrogenation, disproportionation, desorption, and recombination (HDDR) process [37] typically yield the required nanostructures, in which several phases, often of metastable type, can efficiently exchange couple.

12.6.1 Rapidly Quenched $SmCo_5$/Sm_2Co_{17}Magnets

The aforementioned complex aging regime can be simplified when using the melt-spinning method. $Sm(Co_{0.74}Fe_{0.1}Cu_{0.12}Zr_{0.04})_{7.5}$ and $Sm(Co_{0.75}Fe_{0.15}Cu_{0.08}Zr_{0.02})_{7.6}$ ribbons show high coercivities without the lengthy solid solution treatment [105, 107]. Ribbons were produced by melt spinning using a low surface speed of the Cu wheel of 5 m/s and then aged isothermally at 850°C for up to 12 h, followed by slow cooling at 0.7 K/min to different temperatures and then quenched to room temperature. Figure 12.24 (left) shows the room temperature coercivity as a function of isothermal aging time, and it can be seen that the coercivity is sensitive to the alloy composition. A coercivity of above 2.8 T is developed immediately after slow cooling the as-spun $Sm(Co_{0.74}Fe_{0.1}Cu_{0.12}Zr_{0.04})_{7.5}$ sample even without isothermal aging. The coercivity increases with increasing isothermal aging time and a peak

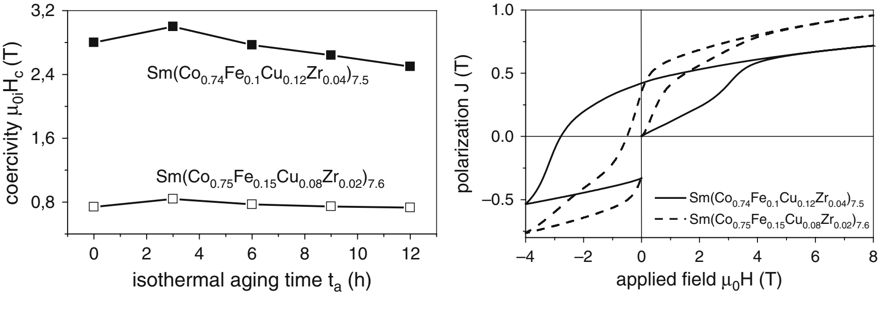

Fig. 12.24 Coercivity μ_{0i} H_c as a function of isothermal aging time at 850°C for $Sm(Co_{0.74}Fe_{0.1}Cu_{0.12}Zr_{0.04})_{7.5}$ and $Sm(Co_{0.75}Fe_{0.15}Cu_{0.08}Zr_{0.02})_{7.6}$ ribbons (*left*). Typical hysteresis loops of the $Sm(Co_{0.74}Fe_{0.1}Cu_{0.12}Zr_{0.04})_{7.5}$ and $Sm(Co_{0.75}Fe_{0.15}Cu_{0.08}Zr_{0.02})_{7.6}$ ribbons subjected to aging at 850°C for 3 h followed by slow cooling to 400°C (*right*). Reproduced with permission of Elsevier from Yan et al. [110]

coercivity of up to 3.0 T can be obtained after aging at 850°C for 3 h, followed by slow cooling to 400°C. For $Sm(Co_{0.75}Fe_{0.15}Cu_{0.08}Zr_{0.02})_{7.6}$ ribbons, however, the coercivity remains almost unchanged around 0.8 T even after a long aging at 850°C followed by a slow cooling to 400°C. A higher Cu and Zr contents promote stronger domain wall pinning and higher coercivity (Fig. 12.24 (right)).

Cu/Zr-poor samples show an incomplete cellular microstructure along with the lamellar phase (Fig. 12.25), underlining that Cu and Zr play very important roles in the formation of the cellular/lamellar microstructure as they modify the phase-ordering kinetics.

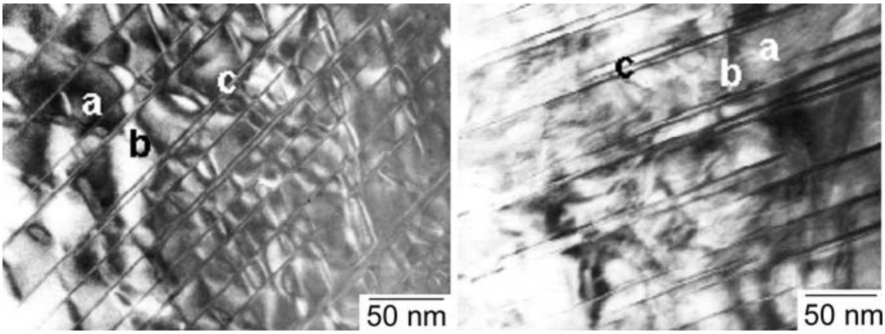

Fig. 12.25 TEM microstructures of annealed ribbons with different Cu and Zr content: *left* – $Sm(Co_{0.74}Fe_{0.1}Cu_{0.12}Zr_{0.04})_{7.5}$; *right* – $Sm(Co_{0.75}Fe_{0.15}Cu_{0.08}Zr_{0.02})_{7.6}$ (a – 2:17-type matrix phase, b – 1:5-type cell boundary phase, and c – lamellar phase). Reproduced with permission of Elsevier from Yan et al. [110]

The formation of a highly twinned, single-phase $TbCu_7$ crystal structure and the supersaturation of Cu and Zr in the matrix phase prior to aging are required to develop the cellular/lamellar microstructure and high coercivity [84]. The structures of as-spun ribbons vary significantly with Cu and Zr contents (Fig. 12.26). The ribbon with high Cu and Zr contents exhibits a single phase with $TbCu_7$ structure. On the other hand, reflections of Th_2Zn_{17} are observed in the Cu/Zr-poor as-spun samples, indicating a mixture of Th_2Zn_{17} and $TbCu_7$ structures.

Magnetically textured $SmCo_5$- [103] and Sm_2Co_{17}-type ribbons can be prepared by single-roller melt spinning at low wheel velocities. The magnetic texture is found to be due to a crystallographic texture formed during the melt-spinning process, with the c-axis parallel to the longitudinal direction of the ribbons. Cu and Zr suppress the formation of a crystallographic texture of 2:17 ribbons prepared at low wheel speed although they are key elements for obtaining the uniform cellular and lamellar microstructures [104–107].

12.6.2 Mechanically Alloyed $SmCo_5/Sm_2Co_{17}$ Magnets

Remanence-enhanced magnet powders consisting of two magnetically hard phases, i.e., $SmCo_5$ and Sm_2Co_{17} nanocomposites, can be prepared by high-energy ball

Fig. 12.26 XRD patterns of as-spun Sm(Co,Fe,Cu,Zr)$_z$ ribbons. Reproduced with permission of Elsevier from Yan et al. [110]

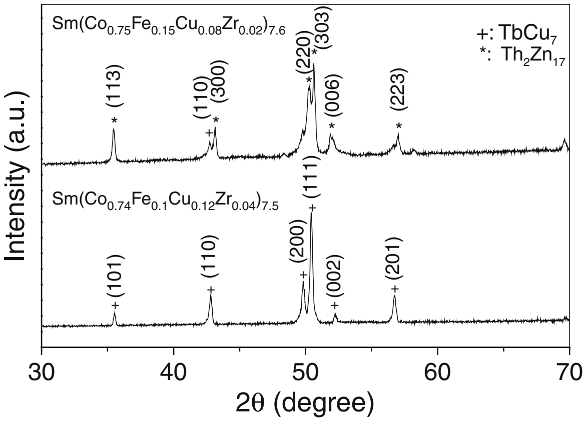

milling and subsequent annealing [104–107]. As-milled powders were found to be amorphous. After annealing, the mean grain sizes of $SmCo_5$, Sm_2Co_{17}, and fcc-Co in the powders determined by the Scherrer method from XRD patterns are about 30, 30, and 35 nm, respectively. The saturation polarization J_s (at 8 T) increases monotonically and the coercivity decreases with increasing volume fraction of Sm_2Co_{17} due to its higher saturation polarization and lower anisotropy field. Consequently, the remanent polarization J_r and the maximum energy density $(BH)_{max}$ first increase and then decrease with the Sm_2Co_{17} volume fraction. The highest remanence of 0.72 T is obtained in the 80% Sm_2Co_{17} powders. Optimum magnetic properties of $J_s = 1.07\,T$, $J_r = 0.67\,T$, $J_r/J_s = 0.63$, $\mu_{0i}\,H_c = 1.56\,T$, and $(BH)_{max} = 78\,kJ/m^3$ are obtained in the mixture consisting of 40% $SmCo_5$ and 60% Sm_2Co_{17}. The relatively low remanence of the nominally 100% Sm_2Co_{17} powder is attributed to its poor coercivity (0.29 T), although the saturation polarization (1.5 T) is much higher than that of rhombohedral Sm_2Co_{17} (which is 1.25 T [95]), due to the presence of elemental fcc-Co. The initial magnetization and demagnetization curves of $SmCo_5/Sm_2Co_{17}$ powders with 0, 60, and 100% Sm_2Co_{17} are shown in Fig. 12.27. All the hysteresis loops show a magnetically single-phase behavior. The smooth demagnetization curves and the enhanced remanence in the two-phase composite can be attributed to the exchange coupling between grains of different phases.

12.6.3 Hydrogen Disproportionated $SmCo_5$ and Sm_2Co_{17} Alloys

For many materials, the conventional HDDR process [37] is not applicable. However, mechanical-induced gas–solid reactions [38] or increased hydrogen pressure [44] can be used to hydrogen disproportionate thermodynamically very stable intermetallic compounds such as those of SmCo type. This reactive milling procedure in enhanced hydrogen pressure and temperature and subsequent vacuum annealing can be employed to first hydrogen disproportionate and second to desorb and recombine the material with the aim to obtain a nanocomposite.

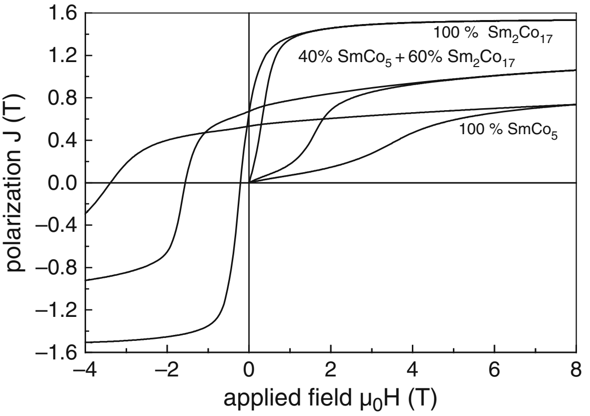

Fig. 12.27 Hysteresis loops of $SmCo_5/Sm_2Co_{17}$ powders with Sm_2Co_{17} volume fraction of 0, 60, and 100%. Reproduced with permission of American Institute of Physics from [104–107]

The effect of reactive milling on Sm_2Co_{17} and as a comparison $Nd_{12}Fe_{82}B_6$ and $Nd_{12}Co_{82}B_6$ is illustrated in Fig. 12.28 (left). The extremely broad reflections of $RH_{2+\delta}$, bcc-Fe, and fcc-Co (note that $SmCo_5$ behaves very similar to Sm_2Co_{17}) indicate a nanocrystalline structure. Lattice strain induced by the milling procedure and stoichiometric inhomogeneities of the hydride phase lead to an additional peak broadening. The average grain size of the $RH_{2+\delta}$ phases is estimated to be around 10 nm. This is a much finer structure than that of disproportionated $Nd_2Fe_{14}B$-type materials [38] prepared by the conventional HDDR method. The desorption curves of the reactively milled powders are shown in Fig. 12.29 (right). Peak (A) in the curves between 100 and 400°C is attributed to the desorption of the δ hydrogen from $RH_{2+\delta}$, whereas peak (B) between 450 and 675°C

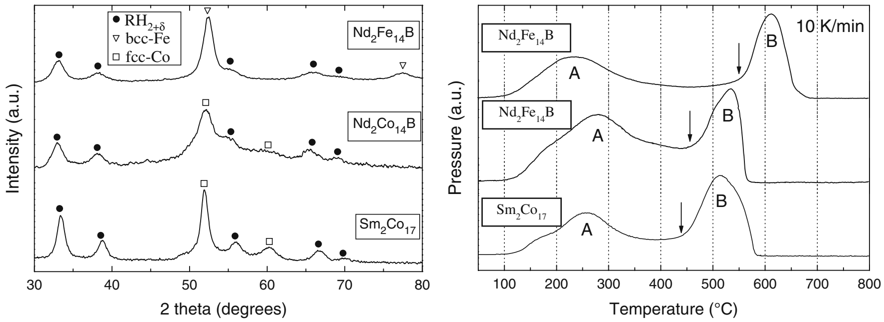

Fig. 12.28 (*left*) XRD patterns of $Nd_{12}Fe_{82}B_6$, $Nd_{12}Co_{82}B_6$, and Sm_2Co_{17} after 20 h (the former) and 40 h (the Co-based alloys) of milling in hydrogen at 350°C. The corresponding disproportionation products are indicated in each case: $RH_{2+\delta}$ with R: Nd, Sm, bcc-Fe, and fcc-Co. (*right*) Desorption behavior of these powders upon heating in vacuum (10 K/min). Peak (A) corresponds to the desorption of the over-stoichiometric hydrogen and peak (B) to the recombination to $Nd_2Fe_{14}B$, $Nd_2Co_{14}B$, and Sm_2Co_{17}, respectively; the *arrows* indicate the onset recombination temperatures

corresponds to the recombination to $Nd_2Fe_{14}B$, $Nd_2Co_{14}B$, and Sm_2Co_{17}. Grain sizes of 20 nm (600°C), 30 nm (700°C), and 100 nm (800°C) are estimated from the XRD patterns for the recombined samples. Thus, reactively milled and subsequently recombined powders show grain sizes much smaller than the average grain size of standard HDDR-treated (around 300 nm) Sm_2Fe_{17}-type and NdFeB-type materials. In fact, grain sizes are rather comparable to those of mechanically alloyed SmCo [101].

Despite the presence of two different phases, the demagnetization curves of the Sm_2Co_{17}-type powders have a magnetically single-phase-like appearance for low recombination temperatures (Fig. 12.29 (left)). The presence of a second phase with a high-anisotropy field is indicated by the gradual approach toward saturation magnetization when recombined at higher temperatures. The remanence $J_r = 0.71$ T for the sample recombined at 600°C is higher than the theoretical maximum value $J_s/2 = 0.65$ T [12] of isotropically distributed single-domain Sm_2Co_{17} particles, which is attributed to the effect of exchange coupling between the nanoscaled grains. It has also to be taken into account that the amount of $SmCo_5$ phase within the sample should decrease the J_r value even further due to the lower value of the saturation magnetization compared to that of Sm_2Co_{17}. An energy product $(BH)_{max} = 82\,kJ/m^3$ was achieved for the sample recombined at 600°C. Figure 12.29 (right) shows that for temperatures below 700°C, a magnetic behavior typical for exchanged coupled magnets can be observed. With decreasing temperature and decreasing grain size, the remanence is enhanced corresponding to a decrease in coercivity. Above 800°C the coercivity decreases for recombination temperatures due to grain growth.

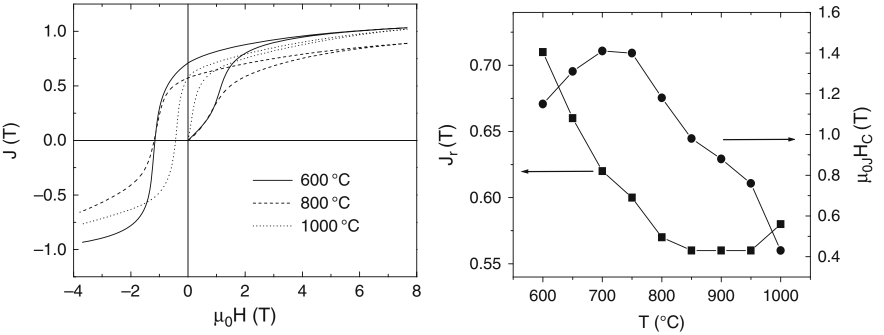

Fig. 12.29 Initial magnetization curves and demagnetization curves of reactively milled Sm_2Co_{17} recombined at different temperatures (*left*). Dependence of remanence J_r and coercivity $\mu_{0i}\,H_c$ of reactively milled Sm_2Co_{17} powders on the recombination temperature T (*right*). Reproduced with permission of American Institute of Physics from [38]

The preparation of highly coercive magnet powders by reactive milling is a novel processing route for the magnetic hardening of compounds, which are highly stabilized toward the reaction with hydrogen and, therefore, disproportionate very sluggishly or, as in the case of NdCoB- and SmCo-type materials, do not react at all under standard HDDR conditions. Nanocrystalline, multiphase but magnetically isotropic SmCo-type powders can be obtained after reactive milling and subsequent recombination at low temperatures. They show a magnetically single phase behavior and enhanced remanences [38].

Acknowledgments Many thanks to *Aru Yan* (then IFW Dresden) for a productive cooperation, to *K.-H. Müller* (IFW Dresden) for fruitful discussion on samarium cobalt magnets and to *L. Schultz* (IFW Dresden) for his continuous support and interest in permanent magnet research.

Acronyms

CEMRP	critical elementary magnetization reversal process
Nano-EDS	nano-beam energy-dispersed spectrometry
HEV	hybrid electric vehicles
HDDR	hydrogenation, disproportionation, desorption, and recombination
HRTEM	high-resolution transmission electron microscopy
MFM	magnetic force microscopy
RPM	rare earth permanent magnets
R–T	rare earth–transition metal compound
SEM	scanning electron microscopy
TEM	transmission electron microscopy
VSM	vibrating sample magnetometer
XRD	X-ray diffraction

References

1. Al-Omari, I.A., J. Shobaki, R. Skomski, D. Leslie-Pelecky, J. Zhou and D.J. Sellmyer. (2002). High-temperature magnetic properties of $\mathrm{SmCo}_{6.7-x}\mathrm{Cu}_{0.6}\mathrm{Ti}_x$ magnets. Physica B: Cond. Matter 321: 107–111.
2. Barthem, V.M.T.S., D. Givord, M.F. Rossignol and P. Tenaud. (2002). An approach to coercivity relating coercive field and activation volume. Physica B 319: 127–132.
3. Buschow, K.H.J. and A.S. van der Goot. (1968). Intermetallic compounds in the system samarium-cobalt. J. Less-Common Met. 14: 323–328.
4. Buschow, K.H.J. and A.S. van der Goot. (1971). Composition and crystal structure of hexagonal Cu-rich rare earth-copper compounds. Acta Cryst. B 27: 1085–1088.
5. Buschow, K.H.J., (1989). Chapter 1, Permanent magnet materials based on 3d-rich ternary compounds. In: Ferromagnetic Materials, vol. 4, E. P. Wohlfarth and K.H.J. Buschow (eds.), North-Holland Elsevier, Amsterdam, Netherlands.
6. Buschow, K.H.J. (1997). Chapter 4, Magnetism and processing of permanent magnet materials. In: Handbook of Magnetic Materials, vol. 10, K.H.J. Buschow (ed.), North Holland Elsevier, Amsterdam, Netherlands.
7. Cataldo, L., A. Lefevre, F. Ducret, M.Th. Cohen-Adat, C.H. Allibert and N. Valignat. (1996). Binary system Sm-Co: revision of the phase diagram in the Co rich field. J. Alloys Comp. 241: 216–223.

8. Chen, C., M.S. Walmer, M.H. Walmer, S. Liu, G.E. Kuhl and G. Simon. (1998). Sm_2(Co, Fe, Cu, Zr)$_{17}$ magnets for use at temperature ≥ 400ºC. J. Appl. Phys. 83: 6706–6708.
9. Chen, C., M.S. Walmer, M.H. Walmer, S. Liu, G.E. Kuhl and G.K. Simon. (1999). New series of Sm_2TM_{17} magnet materials for application at temperatures up to 550°C. In: MRS Symp. Proc. Advanced Hard and Soft Magnets, vol. 577, J. Fidler, M. Coey et al. (eds.), Materials Research Society, Pittsburgh, USA, pp. 277–287.
10. Chen, C., M.H. Walmer, E.H. Kottcamp and W. Gong. (2001). Surface reaction and Sm depletion at 550°C for high temperature Sm-TM magnets. IEEE Trans. Mag. 37: 2531–2533.
11. Chikazumi, S. (1997). Physics of Ferromagnetism, 2nd ed. Oxford Science Publications, Oxford, p. 276.
12. Coey, J.M.D. (ed.). (1996) Rare Earth Iron Permanent Magnets. Clarendon Press, Oxford, UK.
13. Craik, D.J. and E.D. Isaac. (1960). Magnetic interaction domains. Proc. Phys. Soc. (Research Notes) 76.
14. Cullity, B.D. (1972). Introduction to Magnetic Materials. Addison-Wesley Publishing Company, Reading, MA.
15. Delannay, F., S. Derkaoui and C.H. Allibert. (1987a). The influence of zirconium on Sm(CoFeCuZr)$_{7.2}$ alloys for permanent magnets I: identification of the phases by transmission electron microscopy. J. Less-Common Met. 134: 249–262.
16. Delannay, F., S. Derkaoui and C.H. Allibert. (1987b). Transmission electron microscopy of Sm(CoFeCuZr)$_{7.2}$ alloys for permanent magnet. Micron Microscopica Acta 18: 243.
17. Derkaoui, S., C.H. Allibert, F. Delannay and J. Laforest. (1987). The influence of zirconium on Sm(Co,Fe,Cu,Zr)$_{7.2}$ alloys for permanent magnets II: composition and lattice constants of the phases in heat-treated materials. J. Less-Common Met. 136: 75–86.
18. Derkaoui, S. and C.H. Allibert. (1989). Redetermination of the phase equilibria in the system Sm-Co-Cu for Sm content 0–20 at.% at 850°C. J. Less-Common Met. 154: 309–315.
19. Derkaoui, S., N. Valignat and C.H. Allibert. (1996a). Co corner of the system Sm-Co-Zr: decomposition of the phase 1:7 and equilibria at 850°C. J. Alloys Comp. 235: 112–119.
20. Derkaoui, S., N. Valignat and C.H. Allibert. (1996b). Phase equilibria at 1150°C in the Co-rich alloys Sm-Co-Zr and structure of the 1:7 phase. J. Alloys Comp. 232: 296–301.
21. Ding, J., P.G. McCormick and R. Street. (1994). A study of $Sm_{13}(Co_{1-x}Fe_x)_{87}$ prepared by mechanical alloying. J. Magn. Magn. Mat. 135: 200–204.
22. Durst, K.D. and H. Kronmüller. (1985). Magnetic hardening mechanisms in sintered Nd-Fe-B and Sm(Co,Fe,Cu,Zr)$_{7.6}$ permanent magnets. Proc. 4th Int. Symp. Magn. Anisotropy and Coercivity in RETM Alloys, Dayton, USA, pp. 725–735.
23. Durst, K.D., H. Kronmüller, F.T. Parker and H. Oesterreicher. (1986). Temperature dependence of coercivity of cellular Sm_2Co_{17}-$SmCo_5$ permanent magnets. Phys. Stat. Sol. (a) 95: 213–219.
24. Durst, K.D., H. Kronmüller and W. Ervens. (1988a). Investigations of the magnetic properties and demagnetisation processes of an extremely high coercive Sm(Co,Cu,Fe,Zr)$_{7.6}$ permanent magnet – I Determination of intrinsic magnetic material parameters. Phys. Stat. Sol. (a) 108: 403–416.
25. Durst, K.D., H. Kronmüller and W. Ervens. (1988b). Investigations of the magnetic properties and demagnetisation processes of an extremely high coercive Sm(Co,Cu,Fe,Zr)$_{7.6}$ permanent magnet – II The coercivity mechanism. Phys. Stat. Sol. (a) 108: 705–719.
26. Ervens, W. (1979). Rare earth-transition metal 2:17 permanent magnet alloys, state and trends. Goldschmidt Informiert 48: 3–9.
27. Fidler, J. and P. Skalicky. (1982a). Coercivity of precipitation hardened cobalt rare earth 17:2 permanent magnets. J. Magn. Magn. Mat. 30: 58–70.
28. Fidler, J. and P. Skalicky (1982b, September). Domain wall pinning in REPM. In: Proc. 3rd Int. Symp. Magnetic Anisotropy and Coercivity in Rare Earth-Transition Metal Alloys, J. Fidler(ed.), Baden, Austria, pp. 585–597.

29. Gavigan, J.P. and D. Givord. (1990). Intrinsic and extrinsic properties of rare earth-transition metal compounds and permanent magnets. J. Magn. Magn. Mat. 84: 288–298.
30. Givord, D., A. Lienard, P. Tenaud and T. Viadieu. (1987). Magnetic viscosity in Nd-Fe-B sintered magnets. J. Magn. Magn. Mat. 67: L281–L285.
31. Givord, D., P. Tenaud and T. Viadieu. (1988). Coercivity mechanisms in ferrites and rare earth transition metal sintered magnets($SmCo_5$,Nd-Fe-B). IEEE Trans. Magn. 24: 1921–1923.
32. Givord, D., M. Rossignol and V.M.T.S. Barthem. (2003). The physics of coercivity. J. Magn. Magn. Mat. 258–259: 1–5.
33. Goll, D., I. Kleinschroth, W. Sigle and H. Kronmüller. (2000). Melt-spun precipitation-hardened $Sm_2(Co,Cu,Fe,Zr)_{17}$ magnets with abnormal temperature dependence of coercivity. Appl. Phys. Lett. 76: 1054–1056.
34. Goll, D. and H. Kronmüller. (2002). Micromagnetic analysis of pinning-hardened nanostructured, nanocrystalline Sm_2Co_{17} based alloys. Scripta Mat. 47: 545–550.
35. Goll, D., H. Kronmüller and H.H. Stadelmaier. (2004). Micromagnetism and the microstructure of high-temperature permanent magnets. J. Appl. Phys. 96: 6534–6545.
36. Gopalan, R., K. Hono, A. Yan and O. Gutfleisch. (2009). Direct evidence on Cu-concentration variation and its correlation to coercivity in $Sm(Co_{0.74}Fe_{0.1}Cu_{0.12}Zr_{0.4})_{7.4}$ ribbons, Scripta. Mat. 60: 764–767.
37. Gutfleisch, O. and I.R. Harris. (1996). Fundamental and practical aspects of the hydrogenation, disproportionation, desorption and recombination process. J. Phys. D: Appl. Phys. 29: 2255–2265.
38. Gutfleisch, O., M. Kubis, A. Handstein, K.H. Müller and L. Schultz. (1998). Hydrogenation disproportionation desorption recombination in Sm–Co alloys by means of reactive milling. Appl. Phys. Lett. 73: 3001–3003.
39. Gutfleisch, O. (2000). Controlling the properties of high energy density permanent magnetic materials by different processing routes. J. Phys. D: Appl. Phys. 33: R157–R172.
40. Gutfleisch, O., N.M. Dempsey, A. Yan, K.-H. Müller and D. Givord. (2004). Coercivity analysis of melt-spun $Sm_2(Co,Fe,Cu,Zr)_{17.}$ J . Magn. Magn. Mat. 272–276: 647–649.
41. Gutfleisch, O., K.-H. Müller, K. Khlopkov, M. Wolf, A. Yan, R. Schäfer, T. Gemming and L. Schultz. (2006). Evolution of magnetic domain structures and coercivity in high-performance SmCo 2:17 type permanent magnets. Acta Mat. 54: 997–1008.
42. Hadjipanayis, G.C. (1996). Microstructure and magnetic domains. In: Rare-Earth Iron Permanent Magnets, J.M.D. Coey (ed.), Oxford University Press, Oxford, UK, pp. 286–335.
43. Hadjipanayis, G.C., W. Tang, Y. Zhang, S.T. Chui, J.F. Liu, C. Chen and H. Kronmüller. (2000). High temperature 2:17 magnets: relationship of magnetic properties to microstructure and processing. IEEE Trans. Magn. 36: 3382–3387.
44. Handstein, A., M. Kubis, O. Gutfleisch, B. Gebel and K.H. Müller. (1999). HDDR of Sm–Co alloys using high hydrogen pressures. J. Magn. Magn. Mat. 192: 73–76.
45. Handstein, A., A. Yan, G. Martinek, O. Gutfleisch, K.H. Müller and L. Schultz. (2003). Stability of magnetic properties of Sm_2Co_{17}-type magnets at operating temperatures larger than 400ºC. IEEE Trans. Magn. 39: 2923–2925.
46. Hofer, F. (1970). Physical metallurgy and magnetic measurements of $SmCo_5$-$SmCu_5$ alloys. IEEE Trans. Magn. 6: 221–224.
47. Hubert, A. and R. Schäfer (1998). Magnetic Domains – The Analysis of Magnetic Microstructures. Springer Verlag, Berlin, Germany.
48. Kardelky, S., A. Gebert, O. Gutfleisch, A. Handstein, G. Martinek and L. Schultz. (2004). Corrosion behavior of Sm-Co based permanent magnets in oxidizing environments. IEEE Trans. Magn. 40: 2931–2933.
49. Katter, M., J. Weber, W. Assmus, P. Schrey and W. Rodewald. (1996). A new model for the coercivity mechanism of $Sm_2(Co,Fe,Cu,Zr)_{17}$ magnets. IEEE Trans. Magn. 32: 4815–4817.
50. Katter, M. (1998). Coercivity calculation of $Sm_2(Co,Fe,Cu,Zr)_{17}$ magnets. J. Appl. Phys. 83: 6721–6723.

51. Kerschl, P., A. Handstein, K. Khlopkov, O. Gutfleisch, D. Eckert, K. Nenkov, J.-C. Téllez-Blanco, R. Grössinger, K.-H. Müller and L. Schultz. (2005). High-field magnetisation of $SmCo_{5-x}Cu_x$ ($x \approx 2.5$) determined in pulse fields up to 48 T. J. Magn. Magn. Mat. 290–291(part 1): 420–423.
52. Khan, Y. (1973). The crystal structures of R_2Co_{17} intermetallic compounds. Acta Crystall. Section B 29: 2502–2507.
53. Khlopkov, K., O. Gutfleisch, D. Eckert, D. Hinz, B. Wall, W. Rodewald, K.-H. Müller, and L. Schultz. (2004). Local texture in Nd-Fe-B sintered magnets with maximised energy density. J. Alloys Comp. 365: 259–265.
54. Kronmüller, H., K.-D. Durst, W. Ervens and W. Fernengel. (1984). Micromagnetic analysis of precipitation hardened permanent magnets. IEEE Trans. Magn. 20: 1569–1571.
55. Kronmüller, H. and D. Goll. (2002). Micromagnetic theory of the pinning of domain walls at phase boundaries. Physica B 319: 122–126.
56. Kubis, M., A. Handstein, B. Gebel, O. Gutfleisch, K.H. Müller and L. Schultz. (1999). Highly coercive $SmCo_5$ magnets prepared by a modified hydrogenation-disproportionation-desorption-recombination process. J. Appl. Phys. 85: 5666–5668.
57. Kumar, K. (1988). $RETM_5$ and RE_2TM_{17} permanent magnets development. J. Appl. Phys. 63: R13–R57.
58. Lectard, E., C.H. Allibert and R. Ballou. (1994). Saturation magnetization and anisotropy fields in the $Sm(Co_{1-x}Cu_x)_5$ phases. J. Appl. Phys. 75: 6277–6279.
59. Lefèvre, A., L. Cataldo, M.Th. Cohen-Adad, and B.F. Mentzen. (1997). A representation of the Sm-Co-Zr-Cu-Fe quinary system: a tool for optimisation of 2/17 permanent magnets. J. Alloys Comp. 262–263: 129–133.
60. Li, D. and K.J. Strnat. (1984). Domain structures of two Sm-Co-Cu-Fe-Zr “2–17” magnets during magnetization reversal. J. Appl. Phys. 55: 2103–2105.
61. Liu, J.F., T. Chui, D. Dimitrov and G.C. Hadjipanayis. (1998a). Abnormal temperature dependence of intrinsic coercivity in $Sm(Co, Fe, Cu, Zr)_z$ powder materials. Appl. Phys. Lett. 73: 3007–3009.
62. Liu, J.F., Y. Zhang, Y. Ding, D. Dimitrov, and G.C. Hadjipanayis (1998b). Rare earth permanent magnets for high temperature applications. In: Proc. of 15th Int. Workshop on Rare Earth Magnets and their Appl., Dresden, Germany, vol. 2, pp. 607–622.
63. Liu, J.F., Y. Zhang, D. Dimitrov and G.C. Hadjipanayis. (1999). Microstructure and high temperature magnetic properties of $Sm(Co,Cu,Fe,Zr)_z$ ($z = 6.7$–9.1) permanent magnets. J. Appl. Phys. 85: 2800–2804.
64. Livingston, J.D. and M.D. McConnell. (1972). Domain-wall energy in cobalt-rare-earth compounds. J. Appl. Phys. 43: 4756–4762.
65. Livingston, J.D. (1975). Domains in sintered Co-Cu-Fe-Sm magnets. J. Appl. Phys. 46: 5259–5262.
66. Livingston, J.D. and D.L. Martin. (1977). Microstructure of aged $(Co,Cu,Fe)_7Sm$ magnets. J. Appl. Phys. 48: 1350–1354.
67. Matthias, T., G. Zehetner, J. Fidler, W. Scholz, T. Schrefl, D. Schobinger and G. Martinek. (2002). TEM-analysis of $Sm(Co,Fe,Cu,Zr)_z$ magnets for high-temperature applications. J. Magn. Magn. Mat. 242–245: 1353–1355.
68. Maury, C., L. Rabenberg and C.H. Allibert. (1993). Genesis of the cell microstructure in the Sm(Co,Fe,Cu,Zr) permanent magnets with 2:17 type. Phys. Stat. Sol. (a) 140: 57–72.
69. Meyer-Liautaud, F., S. Derkaoui, C.H. Allibert and R. Castanet. (1987). Structural and thermodynamic data on the pseudobinary phases $R(Co_{1-x}Cu_x)_5$ with $R \equiv$ Sm, Y, Ce. J. Less-Common Met. 127: 231–242.
70. Morita, Y., T. Umeda and Y. Kimura. (1987). Phase transformation at high temperature and coercivity of $Sm(Co,Cu,Fe,Zr)_{7\text{-}9}$ magnet alloys. IEEE Trans. Magn. 23: 2702–2704.
71. Nagel, H. (1979). Coercivity and microstructure of $Sm(Co_{0.87}Cu_{0.13})_{7.8}$. J. Appl. Phys. 50: 1026–1030.

72. Nesbitt, E.A., R.H. Willens, R.C. Sherwood and E. Bühler. (1968). New permanent magnet materials. Appl. Phys. Lett. 12: 361–362.
73. Oesterreicher, H., F.T. Parker and M. Misroch. (1979). Giant intrinsic magnetic hardness in $SmCo_{5-x}Cu_x$. J. Appl. Phys. 50: 4273–4278.
74. Ojima, T., S. Tomizawa, T. Yoneyama and T. Hori. (1977). Magnetic properties of new type of rare-earth cobalt magnets. IEEE Trans. Magn. 13: 1317–1319.
75. Panagiotopoulos, I., M. Gjoka and D. Niarchos. (2002). Temperature dependence of the activation volume in high-temperature $Sm(Co,Fe,Cu,Zr)_Z$ magnets. J. Appl. Phys. 92: 7693–7695.
76. Perkins, R.S., S. Gaiffi and A. Menth. (1975). Permanent magnet properties of $Sm_2(Co,Fe)_{17}$. IEEE Trans. Magn. 11: 1431–1433
77. Perkins, R.S. and S. Strässler. (1977). Interpretation of the magnetic properties of pseudobinary $Sm_2(Co,M)_{17}$ compounds. I. Magnetocrystalline anisotropy. Phys. Rev. B 15: 477–489; Interpretation of the magnetic properties of pseudobinary $Sm_2(Co,M)_{17}$ compounds. II. Magnetization. Phys. Rev. B 15: 490–495.
78. Perry, A.J. and A. Menth. (1975). Permanent magnets based on $Sm(Co,Cu,Fe)_z$. IEEE Trans. Magn. 11: 1423–1425.
79. Perry, A.J. (1977). The constitution of copper-hardened samarium-cobalt permanent magnets. J. Less-Common Met. 51: 153–162.
80. Popov, A.G., A.V. Korolev and N.N. Shchegoleva. (1990). Temperature dependence of the coercive force of $Sm(Co,Fe,Cu,Zr)_{7.3}$ alloys. Phys. Met. Metall. 69: 100–106.
81. Rabenberg, L., R.K. Mishra, and G. Thomas. (1982a). Microstructure of precipitation hardened SmCo permanent magnets. J. Appl. Phys. 53: 2389–2391.
82. Rabenberg, L., R.K. Mishra, and G. Thomas. (1982b, September). Development of the cellular microstructure in the $SmCo_{7.4}$-type magnets. In: Proc. 3rd Int. Symp. Magnetic Anisotropy and Coercivity in Rare Earth-Transition Metal Alloys, J. Fidler (ed.), Baden, Austria, pp. 599–608.
83. Ray, A.E. (1984). Metallurgical behavior of $Sm(Co,Fe,Cu,Zr)_z$ alloys. J. Appl. Phys. 55: 2094–2096.
84. Ray, A.E. and S. Liu. (1992). Recent progress in 2:17 type permanent magnets. Proc. 12th Int. Workshop on RE Magnets and their Appl., Canberra, Australia, pp. 552–573.
85. Schobinger, D., O. Gutfleisch, D. Hinz, K.H. Müller, L. Schultz and G. Martinek. (2002). High temperature magnetic properties of 2:17 Sm–Co magnets. J. Magn. Magn. Mat. 242–245: 1347–1349.
86. Schultz, L., K. Schnitzke, J. Wecker, M. Katter and C. Kuhrt. (1991). Permanent magnets by mechanical alloying. J. Appl. Phys. 70: 6339–6344.
87. Skomski, R. (1997). Domain-wall curvature and coercivity in pinning type Sm-Co magnets. J. Appl. Phys. 81: 6527–5629.
88. Skomski, R. and J.M.D. Coey. (1999). Permanent Magnetism. Institute of Physics, Bristol.
89. Skomski, R., A. Kashyap, Y. Qiang, and D.J. Sellmyer. (2003). Exchange through nonmagnetic insulating matrix. J. Appl. Phys. 93: 6477–6479.
90. Stadelmaier, H.H., E.-Th. Henig, G. Schneider and G. Petzow. (1988). The metallurgy of permanent magnets based on $Co_{17}Sm_2$. Z. Metallkd. 79: 313–316.
91. Stadelmaier, H.H., B. Reinsch, and G. Petzow. (1998). Samarium-cobalt phase equilibria revisited; relevance to permanent magnets. Z. Metallkd. 89: 114–118.
92. Stadelmaier, H.H., D. Goll, H. Kronmüller. (2005). Permanent magnet alloys based on Sm_2Co_{17}; phase evolution in the quinary system Sm-Zr-Fe-Co-Cu. Z. Metallkd. 96: 17–23.
93. Streibl, B., J. Fidler and T. Schrefl. (2000). Domain wall pinning in high temperature $Sm(Co,Fe,Cu,Zr)_{7\text{-}8}$ magnets. J. Appl. Phys. 87: 4765–4767.
94. Strnat, K.J., G. Hoffer, J. Olson, W. Ostertag and J.J. Becker. (1967). A family of new cobalt-base permanent magnetic materials. J. Appl. Phys. 38: 1001–1002.

95. Strnat, K.J. (1988). Chapter 2, Rare earth–cobalt permanent magnets. In: Ferromagnetic Materials, vol. 4, E.P. Wohlfarth, K.H.J. Buschow (eds.), North-Holland, Amsterdam, Netherlands.
96. Strnat, K.J. and R.M.W. Strnat. (1991). Rare earth–cobalt permanent magnets. J. Magn. Magn. Mat. 100: 38–56.
97. Tang, H., Y. Liu and D.J. Sellmyer. (2002). Nanocrystalline $Sm_{12.5}(Co,Zr)_{87.5}$ magnets: synthesis and magnetic properties. J. Magn. Magn. Mat. 241: 345–356.
98. Tang, W., Y. Zhang and G.C. Hadjipanayis. (2000). Effect of Zr on the microstructure and magnetic properties of $Sm(Co_{bal}Fe_{0.1}Cu_{0.088}Zr_x)_{8.5}$ magnets. J. Appl. Phys. 87: 399–403.
99. Tang, W., A.M. Gabbay, Y. Zhang, G.C. Hadjipanayis and H. Kronmüller. (2001). Temperature dependence of coercivity and magnetisation reversal in $Sm(Co_{bal}Fe_{0.1}Cu_yZr_{0.4})_{7.0}$ magnets. IEEE Trans. Magn. 37: 2515–2517.
100. Walmer, M.S., C.H. Chen and M.H. Walmer. (2000). A new class of Sm-TM magnets for operating temperatures up to 550°C. IEEE Trans. Magn. 36: 3376–3381.
101. Wecker, J., M. Katter and L. Schultz. (1991). Mechanically alloyed Sm-Co materials. J. Appl. Phys. 69: 6058–6060.
102. Xiong, X.Y., T. Ohkubo, T. Koyama, K. Ohashi, T. Tawara and K. Hono. (2004). The microstructure of sintered $Sm(Co_{0.72}Fe_{0.20}Cu_{0.055}Zr_{0.025})_{7.5}$ permanent magnet studied by atom probe. Acta Mat. 52: 737–748.
103. Yan, A., W.-Y. Zhang, H.-W. Zhang and B. Shen. (2000). Melt-spun magnetically anisotropic $SmCo_5$ ribbons with high permanent performance. J. Magn. Magn. Mat. 210: 10–14.
104. Yan, A., A. Bollero, O. Gutfleisch and K.H. Müller. (2002a). Microstructure and magnetization reversal in nanocomposite $SmCo_5/Sm_2Co_{17}$ magnets. J. Appl. Phys. 91: 2192–2196.
105. Yan, A., A. Bollero, K.-H. Müller and O. Gutfleisch. (2002b). Fast development of high coercivity in melt-spun $Sm(Co,Fe,Cu,Zr)_z$ magnets. Appl. Phys. Lett. 80: 1243–1245,
106. Yan, A., A. Bollero, K.H. Müller and O. Gutfleisch. (2002c). Influence of Fe, Zr and Cu on microstructure and crystallographic texture of melt-spun 2:17 SmCo ribbons. J. Appl. Phys. 91: 8825–8827.
107. Yan, A., K.H. Müller and O. Gutfleisch. (2002d). Highly coercive melt-spun $Sm(Co, Fe, Cu, Zr)_z$ magnets prepared by simple processing. IEEE Trans. Magn. 38: 2937–2939.
108. Yan, A., O. Gutfleisch, T. Gemming and K.-H. Müller. (2003a). Microchemistry and reversal mechanism in 2:17-type Sm-Co magnets. Appl. Phys. Lett. 83: 2208–2210.
109. Yan, A., O. Gutfleisch, A. Handstein, T. Gemming and K.-H. Müller. (2003b). Microstructure, microchemistry, and magnetic properties of melt-spun $Sm(Co,Fe,Cu,Zr)_y$ magnets. J. Appl. Phys. 93: 7975–7977.
110. Yan, A., A. Bollero, O. Gutfleisch, K.-H. Müller, L. Schultz, (2004). Melt-spun precipitation hardened $Sm(Co,Fe,Cu,Zr)_z$ magnets, Mat. Sci. Eng. A375–377: 1169–1172.
111. Yang, W., W. Ping, S. Zhenhua and Z. Shouzeng. (1992). 2:17 type temperature compensated magnets with high coercivity. In: Proc. of the 12th Int. Workshop on RE Magnets and their Appl., Canberra, Australia, pp. 249–257.
112. Zhang, Y., W. Tang. G.C. Hadjipanayis, C. Chen, C. Nelson and K. Krishnan. (2000). Evolution of microstructure, microchemistry and coercivity in 2:17 type Sm–Co magnets with heat treatment. IEEE Trans. Magn. 37: 2525–2527.
113. Zhou, J., I.A. Al-Omari, J P. Liu and D.J. Sellmyer. (2000). Structure and magnetic properties of $SmCo_{7-x}Ti_x$ with $TbCu_7$-type structure. J. Appl. Phys. 87: 5299–5301.
114. Zhou, J., R. Skomski, and D.J. Sellmyer. (2003). Magnetic hysteresis of mechanically alloyed Sm–Co nanocrystalline powders. J. Appl. Phys. 93: 6495–6497.